Multi-scale seismic imaging of the Ridgecrest, CA, region with full-waveform inversions of regional and dense array data

Guoliang Li[1], Yehuda Ben-Zion[1]

[1]Department of Earth Sciences and Statewide California Earthquake Center, University of Southern California, Los Angeles, CA, USA

Abstract

We develop a methodology for deriving multi-scale velocity models with waveform inversions of earthquake and ambient noise data recorded by regional and dense sensor configurations. The method is applied for the area around the 2019 Ridgecrest earthquake rupture zones, utilizing data recorded by regional stations and dense 2D and 1D arrays with station spacings of ~5 km and ~100 m, respectively. Starting with regional Vp, Vs models and locations of Ridgecrest aftershocks, the velocity models and event locations are improved iteratively by inversions of waveforms recorded by regional stations and the 2D array, using a minimum Gauss-Lobato-Legendre (GLL) distance of ~150 m. Waveforms from local events recorded by dense 1D arrays across the M7.1 rupture zone with high SNR for frequencies of 10 Hz are used to resolve small-scale features of the rupture zone and shallow crust with a local GLL point distance of 20 m. The refined models provide self-consistent descriptions of the rupture zone and the shallow crust embedded in the regional structures. The results reveal pronounced low Vs and high Vp/Vs in the M6.4 and M7.1 rupture zones coinciding with concentrations of seismicity, and also around the Garlock fault and in several local basins. We also observe clear velocity contrasts across the Garlock fault with polarity reversals along strike ands with depth. The obtained multi-scale velocity models can be used to improve derivations of earthquake source properties, simulations of dynamic ruptures and ground motions, and the understanding of fault and tectonic processes in the region.

Key Points

1. We develop a workflow for deriving multi-scale Vp and Vs models with full-waveform inversions of data from hierarchical seismic networks.
2. Application for the Ridgecrest region provides self-consistent descriptions of the rupture zones within the context of regional structures.
3. The results resolve the damaged zones as low Vs and high Vp/Vs anomalies, and spatially-variable velocity contrasts across the Garlock fault

Plain Language Summary

Seismic velocity models are foundational for a wide range of topics including clarifying properties of subsurface and fault zone structures, derivation of earthquake source properties, and simulations of ruptures and seismic ground motions. Typical imaging studies are done at given spatial scales and resolutions related to the used seismic network. Here we develop a methodology for multi-scale multi-resolution tomographic waveform imaging using data recorded by regional and local denser seismic networks. Application of the methodology to seismograms recorded in the region around the 2019

Ridgecrest earthquake sequence provide detailed information about seismic velocities in the main earthquake rupture zones and the shallow crust, embedded within a regional context. The results highlight anomalous ratios of P-to-S wave velocities in the rupture zones indicative of rock damage and possibly enhanced by fluids, along with spatially-variable contrast of shear wave velocities across the Garlock fault in the area. The results advance the ability to perform future observational research and numerical simulations of earthquake processes in the area. The developed methodology can be used to derive multi-scale velocity models at other locations.

1. Introduction

Seismic imaging studies usually focus on one dominant scale (e.g., global, regional, exploration, fault zone, etc.) associated with given distributions of stations and frequency bands of the input seismic data. There are currently several regional seismic velocity models in southern California (e.g., Lee et al., 2014; Shaw et al. 2015; Fang et al., 2022), but validation studies show that they have poor resolution at the top 1-3 km of the crust and around large fault zones due to the lack of using high-frequency data (e.g., Lu & Ben-Zion, 2022). In various places there are higher resolution velocity models for the shallow crust and around fault zones (e.g. Lin et al., 2013; Allam et al., 2014; Mordret et al., 2019; Zigone et al.., 2019; Ajala et al., 2019). However, combining velocity models of different scales is challenging and may produce artifacts even at large distances from the boundaries of embedded smaller-scale higher resolution models (e.g. Juarez & Ben-Zion, 2020; Ajala and Persaud, 2021). Indeed, simulations of ground motion using regional models that include embedded fault zone structures and detailed information for the top crust demonstrate the profound effects of these small-scale features on the regional-scale seismic wavefield (Yeh & Olsen, 2023; Schliwa et al., 2023; Callaghan et al., 2023). It is thus important to develop techniques that can produce multi-scale velocity models that are not affected by artificial boundaries between separately-derived models. This requires using data recorded at a range of frequency bands by multi-scale configurations of seismic stations and an appropriate multi-scale inversion methodology.

After the 2019 M6.4 and M7.1 Ridgecrest earthquakes in Southern California, dense 2D and 1D arrays of sensors were deployed in the area with station spacings of ~5 km and ~100 m, respectively (Catchings et al., 2020). These arrays, combined with stations of the regional seismic network, provide hierarchical data that can be used to derive seamless multi-scale P and S velocity models. In the present paper, we develop and use an iterative procedure to perform full waveform tomographic imaging on both the regional and fault zone scales for the crustal volume around the main rupture zones of the Ridgecrest earthquake sequence. The method first refines the initial regional velocity models via waveforms of aftershocks and noise-based Green's functions using data within a period band of 8-0.3 s recorded by the 2D regional array. Using the refined regional models and relocated events, finer-scale fault-zone models are further derived from local earthquake waveforms within a higher frequency band of 1-10 Hz recorded by the linear arrays. The regional velocity models resolve clear low Vs and high Vp/Vs anomalies to depths of up to 6 km at basins in the area as well as along the Garlock fault and rupture zones of the main 2019 Ridgecrest earthquakes. The fault zone modes reveal additional details of the low velocity zones and high Vp/Vs anomalies under the mapped surface ruptures, along with correlations between the high Vp/Vs anomalies and concentration of seismicity.

In the next section we describe the seismic waveform data sets used in the study and basic processing of the recorded earthquake waveforms and ambient seismic noise. In section 3 we provide an overview of our strategy for deriving multi-scale velocity models, leaving technical details for the supplementary information. In section 4 we describe the derived results, starting with the regional Vp, Vs, and Vp/Vs models and continuing with finer-scale results for the main rupture zones and the top crust below the dense linear arrays. The obtained velocity models include detailed structures of the rupture zones and the subsurface embedded self-consistently in the regional model. In section 5 we discuss further the results including velocities along vertical profiles across the M7.1 rupture zone and velocity contrasts across the Garlock fault, and provide suggestions for continuing future studies.

2. Data and basic processing

Following the 2019 Mw6.4 and Mw7.1 Ridgecrest, California earthquakes, researchers from the USGS and SCEC deployed approximately 480 three-component nodal seismic sensors about 2 months in the area (Catchings et al., 2020). The deployment included two subarrays forming rectangular grids, with an average inter-station distance of about 5 km, covering primarily the rupture zones of the large events and Garlock fault. Additionally, 4 fault-perpendicular linear arrays with an inter-station distance of around 100 m were established along the main rupture zone of the Mw 7.1 earthquake. Furthermore, 50 broadband stations from various other 2D arrays and regional networks (e.g., CI, GS, ZY) were also operational in this region. Throughout the observational period, these 2D and dense 1D arrays continuously recorded ambient noise and captured thousands of aftershocks that can be utilized to construct multi-scale regional and fault-zone velocity models. Figure 1 displays the station locations in relation to key tectonic elements (e.g., the main ruptures of the M6.4 and M7.1 Ridgecrest events and the Garlock fault) and the boundaries of major geological provinces. The seismic waveforms recorded by the various arrays and regional stations are used below to derive multi-scale Vp and Vs models for the Ridgecrest area.

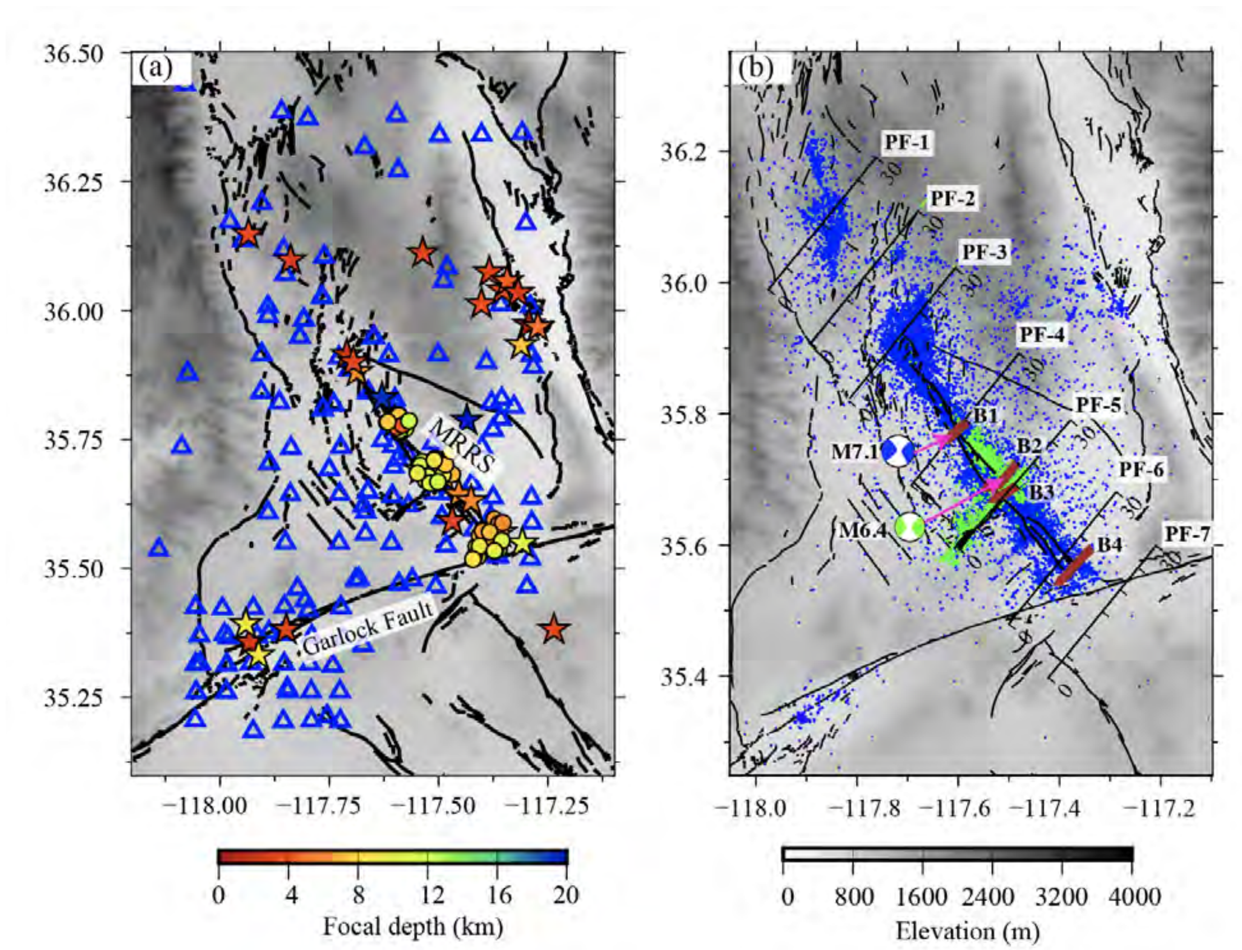

Figure 1: (a) The study area and 2D seismic stations. Surface fault traces are shown as black lines, including the Garlock Fault (GF) and the Main Ruptures of the 2019 Ridgecrest Sequence (MRRS). The stars and circles mark events selected for building the regional and fault-zone scale models, respectively, with depth denoted by the color scale below. The background map shows elevation downloaded from Open Topography. (b) Zoom-in of the main ruptures of the 2019 Ridgecrest sequence. Events between the Mw 6.4 and Mw 7.1 and within 50 days after the Mw 7.1 mainshock are plotted with green and blue colors. Sensors of the four dense linear arrays (B1-B4) crossing the main rupture of the Mw 7.1 mainshock are represented as brown triangles. The seven black lines PF1-PF7 mark the locations of vertical velocity profiles shown in Figures 11 and S5.

2.1 Earthquake waveforms

White et al. (2021) derived a local travel time tomography and an earthquake catalog with about 95,000 events for the Ridgecrest sequence utilizing data from both the regional and dense 2D arrays. The nominal location errors of events in the White et al. (2021) catalog are about 1 km horizontally and vertically. From this catalog, we selected 29 events evenly distributed throughout the study area (Figure 1a and supporting information table S1) to be used for updating the regional velocity model. To build fine-scale fault-zone images, we further selected around 74 events with magnitude above 1.8 (see Figure 1a; supporting information table S2) primarily located beneath the dense 1D arrays. The data processing of event waveforms consists of removing the mean and discarding waveforms with an SNR below 5. The SNR is defined as the maximum envelope amplitude of P-waveforms divided by the root-mean-square of noise within a time window spanning 20 sec and starting 30 sec before the P-wave arrival time.

Figure 2a illustrates the waveforms of an event with a magnitude of 2.5 recorded by the regional 2D arrays. Even within a high frequency band of 0.3-10 Hz, the waveforms exhibit high-quality P- and S-wave signals, which can be utilized to constrain the upper several hundred meters of the velocity structure in the regional model. Figure 2b depicts the waveforms of a smaller event with a magnitude of 2.0 recorded by the nearby linear B4 array. Due to the small epicentral distance of approximately 10 km, high quality P- and S-wave signals are observed up to 20 Hz, which allow in principle of resolving velocity heterogeneities on scales as small as tens of meters.

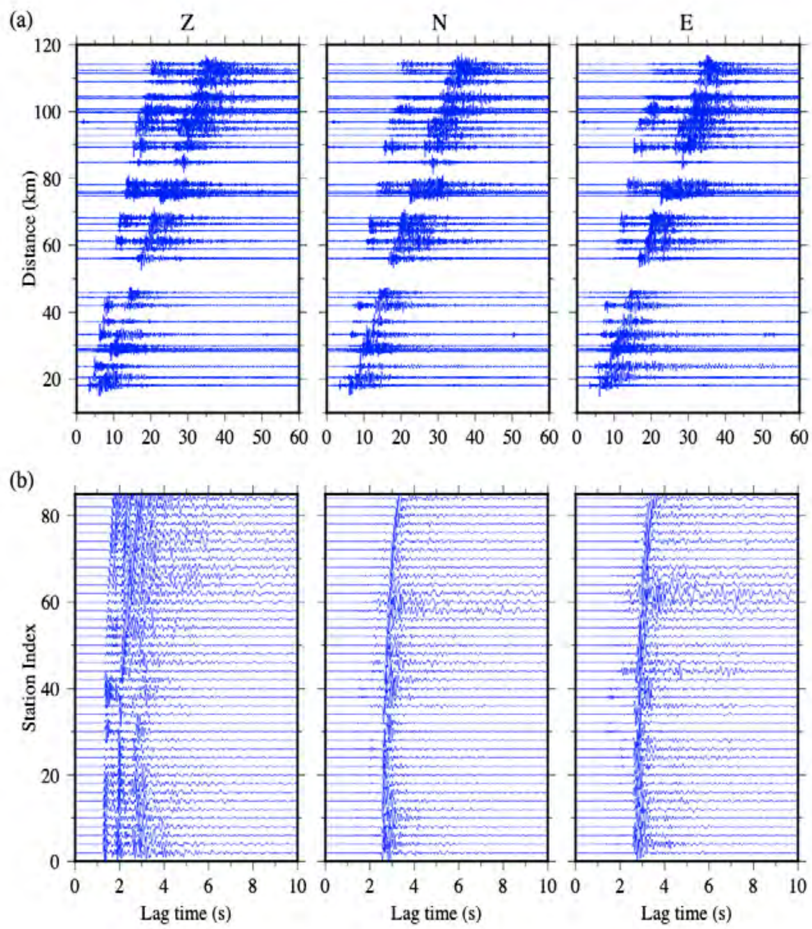

Figure 2: (a) An example of one event with a magnitude of 2.5 recorded by 2D arrays. The waveforms are filtered at a frequency band of 0.3-10 Hz (b) An example of one event with a magnitude of 2.0 recorded by the B4 linear array. The waveforms are filtered at a frequency band of 1-20 Hz.

2.2 Extracting surface waves from noise correlations

Rayleigh wave signals in the period band of 8–3 sec are extracted from cross-correlations of the ambient seismic noise. The data processing procedures are based largely on the methods described by Shapiro et al. (2005), Bensen et al. (2007), and Li et al. (2021). The analysis includes the following main steps. First, we divide the continuous data into daily time series and remove the mean, trend, and instrumental responses. Secondly, we apply temporal normalization and spectral whitening to suppress strong transient signals such as earthquakes and flatten the noise spectrum. Thirdly, we perform Z-Z component noise cross-correlations on a daily basis for all 2D station arrays with overlapping time intervals of ~23 days. To enhance the Signal-to-Noise ratio, we further stack these daily noise cross-correlation functions using the time-frequency phase weighted stacking method (tf-PWS) described by Li et al. (2018). This method has demonstrated better denoising efficiency compared to linear stacking while preserving the dispersive characteristics of the stacked waveforms. The causal and anticausal components of these non-linearly stacked cross-correlations are combined to improve the SNR and mitigate the influence of heterogeneous noise distribution, resulting in symmetric cross-correlations. Finally, we extract Empirical Green's Functions (EGFs) between pairs of stations by computing the negative time derivatives of the ambient noise cross-correlations (Figure 3). The obtained EGFs in the period band of 8–3 sec are utilized to update the regional velocity model in the Ridgecrest region.

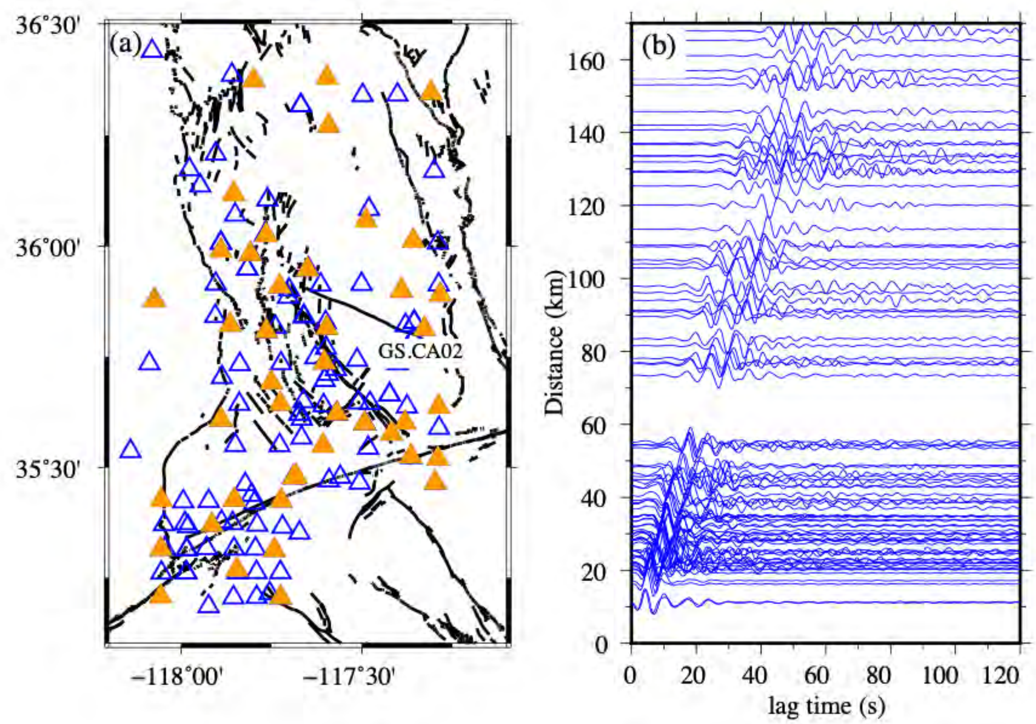

Figure 3: (a) The triangles represent regional 2D stations used to extract EGFs and the Orange ones show the locations of selected stations as virtual sources. (b) An example shows one trace of extracted EGFs band passed with a virtual source of GS.CA02. The location of the virtual source is marked in (a) and the waveforms are filtered within a period band of 8-3 s.

3. Multi-Scale Imaging Methodology

To conduct inversions of seismic waveforms recorded by the hierarchical distributions of sensors in the regional network, 2D arrays, and 1D arrays, we use the following strategy addressing two imaging scales (Figure 4). We first employ long-period EGFs based on noise correlations in the period range of 3-8 sec to refine the initial regional velocity models. We aim to obtain an intermediate regional model that provides sufficient accuracy for relocating 29 regional events. Then, the intermediate velocity model is further updated using the waveforms of the relocated 29 earthquakes with an intermediate period range spanning 3-0.3 sec. Subsequently, leveraging the enhanced regional velocity models as new initial references, we further use high-frequency body waveforms (1-10 Hz) acquired from the 1D linear arrays to iteratively relocate again the used events and derive updated detailed structures of fault zones and the shallow crust. The workflows for both imaging scales are illustrated and explained in the subsequent sections.

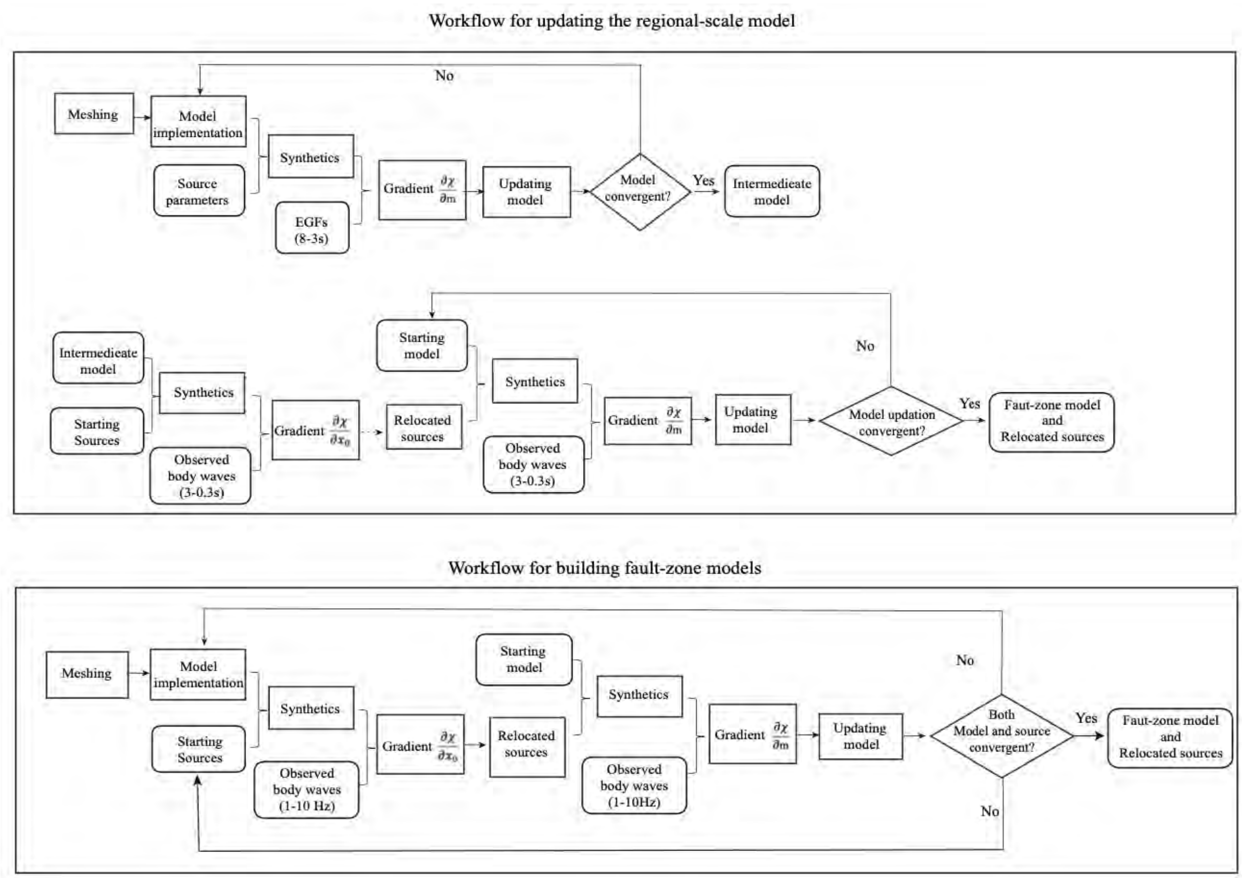

Figure 4: Workflows for developing multi-scale regional and fault-zone velocity models.

3.1 Updating regional-scale velocity models using 2D arrays

We start the process by constructing a regional mesh using the Cartesian Meshing Spherical Earth tool (CMSE) (Li et al., 2022). The CMSE meshing tool can accurately account for the spherical earth curvature and the surface topography, and it uses a user-friendly local cartesian coordinate, which makes it more accurate and convenient than the built-in meshing tool of the SPECFM3D_cartesain package to build the regional mesh (Li et al., 2022). For the top 5 km, the resulting regional mesh consists of 240 elements in latitude (150 km), 160 elements in longitude (100 km), and 8 elements in depth. Considering that the wave speeds increase with depths, the length of elements is doubled for depths greater than 5km to save storage and computational cost. This configuration yields a total element number of approximately 0.6 million. As each mesh consists of 5×5×5 Gauss-Lobato-Legendre (GLL) points, the smallest GLL point distance is ~150 m on the surface, which gives sufficient simulation accuracy at periods of 0.3 s and longer assuming a minimum wave speed of 1.0 km/s. Figure 5a shows the built regional mesh and illustrates the incorporation of surface topography that makes the simulation volume more realistic.

To alleviate local minimum pitfalls and increase the convergence rate of inversion, we chose for initial Vp and Vs models the tomographic results of Fang et al. (2022), which were shown to outperform other velocity models (CVMS-4.26, CVMH-15.1) in the Ridgecrest region. The mass density is calculated from the Vp values of Fang et al. (2022) using the empirical Law of Brocher (2005):

$$\rho = 1.6612Vp - 0.4721Vp^2 + 0.0671Vp^3 - 0.00431Vp^4. \quad (1)$$

The Qs and Qp coefficients are derived from the Vs and Vp/Vs values using the following empirical relations (Brocher 2005; Olsen et al., 2003):

$$Q_s = 10.5 - 16Vs + 153Vs^2 - 103Vs^3 + 34.7Vs^4 - 5.29Vs^5 + 0.31Vs^6, \quad (2)$$

$$Q_p = \frac{3}{4}(Vp/Vs)^2 Q_s. \quad (3)$$

As depicted in the top flowchart of Fig. 4, the regional scale imaging involves several types of data and steps. We first use the long-period surface wave to generate an intermediate regional model. Then, the intermediate model is used to perform earthquake relocations and subsequent model updates that utilize earthquake waveforms from the 2D arrays. To simulate Rayleigh-wave waveforms $\boldsymbol{u}(\boldsymbol{x}, t)$, single vertical point sources are placed at the locations of virtual sources while all other stations are treated as receivers. A Gaussian function is used as the source time function of point forces:

$$\boldsymbol{f}(t) = \frac{1}{\sqrt{\pi}\tau} e^{-(\frac{t}{\tau})^2}, \quad (4)$$

where τ is the half-duration of the source, which is set as 1.0 s since the synthetics are further filtered. The highly accurate spectral element method (Graves, 1996; Robertsson, 1996; Komatitsch and Tromp, 1999) is employed to solve the forward modeling and adjoint simulations in the 3D heterogeneous velocity models.

The waveforms of synthetics and EGFs within a period band of 3-8 s are used to construct the cross-correlation based traveltime misfit function:

$$\chi(\boldsymbol{m}, \boldsymbol{s}) = \sum_{i=1}^{N} \sum_{k=1}^{K} w_{i,k} \left[T_{i,k}^{obs} - T_{i,k}^{syn}(\boldsymbol{m}, \boldsymbol{s})\right]^2 \quad (5)$$

where, $T_{i,k}^{obs}$ denotes the observed travel time of the *i*th and *k*th source-receiver combination, and $T_{i,k}^{syn}(\boldsymbol{m}, \boldsymbol{s})$ represents the predicted travel time based on the current model ***m*** and source ***s***. Here, *N* and *K* are the numbers of used events and stations, and $w_{i,k}$ is a weight term determined by the SNR, waveform similarity and time-shift. The detailed definition of $w_{i,k}$ is provided in the supplementary text S1. Since the locations of the virtual sources are known, only the velocity model ***m*** is updated at this stage.

The adjoint method is used to calculate the gradient of the misfit function with respect to model parameters ($\frac{\partial \chi}{\partial \boldsymbol{m}}$) by correlating the forward wavefield $\boldsymbol{u}(\boldsymbol{x}, t)$ and the adjoint wavefield $\boldsymbol{u}^{\dagger}(\boldsymbol{x}, T-t)$ (e.g., Tarantola ,1984; Tromp et al., 2005; Fichtner et al., 2006; Liu et al., 2006). A detailed description of the methodology is provided in the supplementary Text S2. The adjoint wavefield $\boldsymbol{u}^{\dagger}(\boldsymbol{x}, T-t)$ is generated by the time-reversed adjoint sources $\boldsymbol{f}^{\dagger}$ injected at receivers with a form of $\boldsymbol{f}^{\dagger}(\boldsymbol{x}, t) = \delta t \cdot \dot{\boldsymbol{u}}(\boldsymbol{x}, T-t)$ determined by the misfit function in equation (5). At each iteration, the current velocity model is updated along the negative direction of the gradient, and the linear search method is used to decide the optimal step length α. Iterations terminate when the misfit reduction becomes minor, generating the intermediate regional velocity model.

Next, the intermediate regional model is used to update the source parameters of the used earthquakes. The initial source locations $\boldsymbol{x_0}$, starting time t_0 and focal mechanism $\boldsymbol{M}$ are taken from the seismicity and focal mechanism catalogs White et al. (2021) and Cheng et al. (2023), respectively. To synthesize synthetic displacement seismograms $\boldsymbol{u}(\boldsymbol{x}, t; \boldsymbol{x_0}, M)$ generated by an impulsive point source located at $\boldsymbol{x_0}$ with a moment tensor $\boldsymbol{M}$, we use the following equation (Aki and Richards, 2022):

$$\boldsymbol{u}(\boldsymbol{x}, t; \boldsymbol{x_0}, \boldsymbol{M}) = \boldsymbol{G}(\boldsymbol{x}, t; \boldsymbol{x_0}, \boldsymbol{M}) * \boldsymbol{f}(t - t_0; \tau), \qquad (6)$$

where $\boldsymbol{f}(t - t_0; \tau)$ denotes the source time function defined by equation (4). The half-duration τ is estimated as 0.03 s for events with magnitudes of 2-3 with an assumption of rupture speed of 3 km/s (Ben-Zion, 2008).

To relocate the source position of *i* th event, we calculate the misfit gradient $\frac{\partial \chi_i}{\partial \boldsymbol{x_0}}$ by the adjoint method using the detailed derivations described in Text S2 (e.g., Liu et al., 2006; Kim et al., 2011), and then perturb the location by a small amount ϵ along the negative direction to get the perturbations in the Green's function:

$$\delta_{\epsilon}\boldsymbol{G} = \boldsymbol{G}\left(\boldsymbol{x}, t;\ \boldsymbol{x_0} - \epsilon \cdot \frac{\delta \chi_i}{\delta x_0},\ \boldsymbol{M_0}\right) - \boldsymbol{G}(\boldsymbol{x}, t;\ \boldsymbol{x_0},\ \boldsymbol{M_0}). \qquad (7)$$

By assuming a linear relationship between the small amount of the location shift and waveform perturbations (e.g., Warner et al., 2013; Tao et al., 2018), the perturbed waveforms of step α can be approximated as:

$$\boldsymbol{u}(\boldsymbol{x}, t, a) \approx (\boldsymbol{G} + \alpha \cdot \epsilon^{-1} \delta_{\epsilon}\boldsymbol{G}) * \boldsymbol{f}(t - t_0, \tau). \qquad (8)$$

The optimal step length α is obtained by minimizing the misfit function of equation (5). To save computational time, we only conduct source locations once in the regional-scale inversion. The relocated events are further used to iteratively update the regional-scale velocity model with a similar procedure as described for using EGFs to update results. The structural inversion terminates when the residual reduction becomes minor, producing the final regional-scale velocity model.

3.2 Deriving fault-zone scale structures using dense linear arrays

In the fine-scale imaging stage (bottom flowchart in Fig. 4), we use data recorded by the B1-B4 linear arrays (perpendicular to the rupture of the Ridgecrest mainshock) to invert for detailed structures of the rupture zone and shallow crust. We start again with meshing the simulation volumes using now much finer meshes. Figure 5b shows an example for a fine mesh centered around the B4 array with horizontal dimensions of 16 km×16 km and vertical extent of 15 km. In the top 2 km, the simulation volume has 208×208 elements in the lateral directions and 23 elements in the vertical direction. With increasing depth, the lengths of the elements are doubled twice at depths of 2 km and 6 km. The total number of spectral elements is about 1.3 million, with the smallest inter-GLL distance of about 20 m. As B2 and B3 are spatially close to each other, we combine the two arrays and build a joint mesh for both. The meshes for arrays B1 and B2-B3 are shown in Figure S1. This set of fine meshes can be used to simulate seismograms with frequency up to 15 Hz.

The workflow of building fine-scale models for fault-zones and the shallow crust is similar to that of using body waves to update the regional-scale model, except that the source locations and velocity models are updated in consecutive iterations. The final regional velocity model is used here as the initial model, and the initial source parameters ($\boldsymbol{x_0}$, t_0, $\boldsymbol{M}$) are taken as before from the catalogs of White et al. (2021) and Cheng et al. (2023). At each iteration, recorded waveforms and synthetics are compared in a high frequency band of 1-10 Hz, and used to calculate gradients with respect to source locations ($\frac{\partial \chi_i}{\partial \boldsymbol{x_0}}$). Equations (7) and (8) are used to improve the event locations based on the current velocity model. After that, the relocated events are used to generate synthetic waveforms and compared again with the observed waveforms. With the same definition of misfit function (equation 5) and same format of adjoint source equation, the gradient with respect to model parameters $\frac{\partial \chi}{\partial \boldsymbol{m}}$ is calculated and used to update the current velocity model. The whole process continues until both source locations and the velocity model converge.

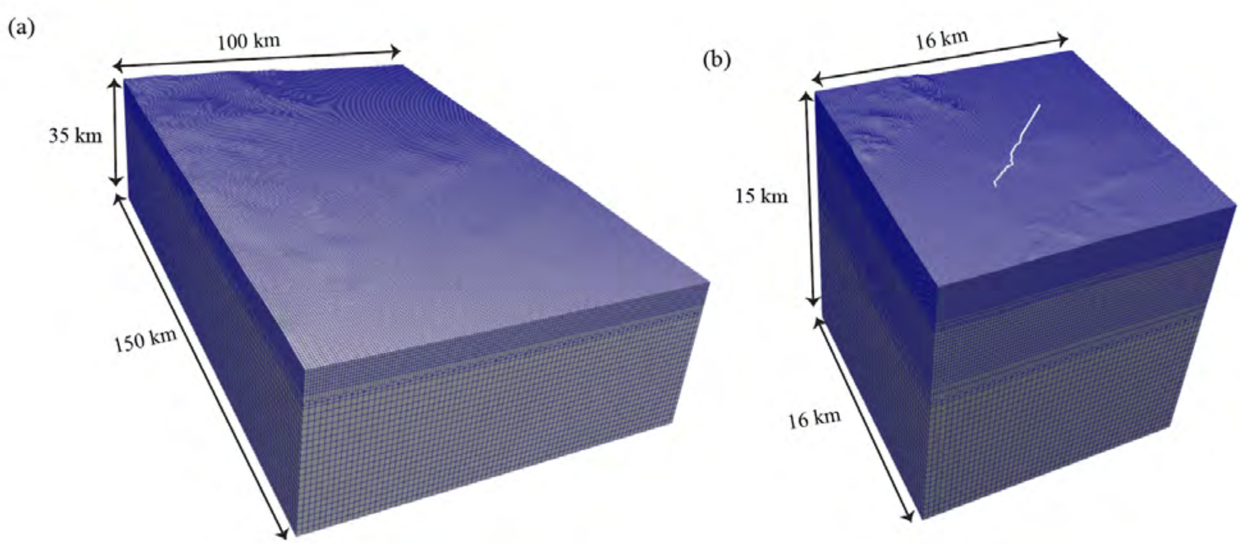

Figure 5: (a) The mesh for the regional volume. (b) The built mesh for the volume around the B4 array with white dots representing stations of the linear array.

4. Results

4.1 Regional velocity model

In this section, we first present the improvements of Rayleigh wave misfit. For the initial model, hereinafter referred as Model-0, there is a mean travel-time residue of ~1.08 s (Figure 6a). The distribution of the residues is further shown in Figure 6b. With the definition of equation (5), the positive average indicates that the synthetic waveforms are overall advanced with respect to the observed waveforms, meaning that the initial model is generally faster than the ground-truth data. After 6 iterations, the average misfit reduces to 0.13 s, with a reduction of 88%. As the misfit reduction becomes small at the last two interactions, we terminate further iterations using Rayleigh waves and converge on an intermediate regional model named as the Model-6. The histogram of misfits for this model is plotted in Figure 6c.

Using Model-6 we relocated the 29 events and listed the relocated catalog in supporting materials. Then P- and S-waves from the 29 events are further used to update the regional model. As Figure 6d shows, the Model-6 is still slightly faster than the crust, with a mean residue of 0.28 s. After additional six iterations, the misfit reductions become considerably smaller (Figure 6d) and we terminate the updates obtaining the final regional velocity model named Model-12. Figures 6e and 6f show the histograms of the body wave travel-time residues of Model-6 and Model-12, respectively, and Table S1 summarizes the updated locations of the 29 events.

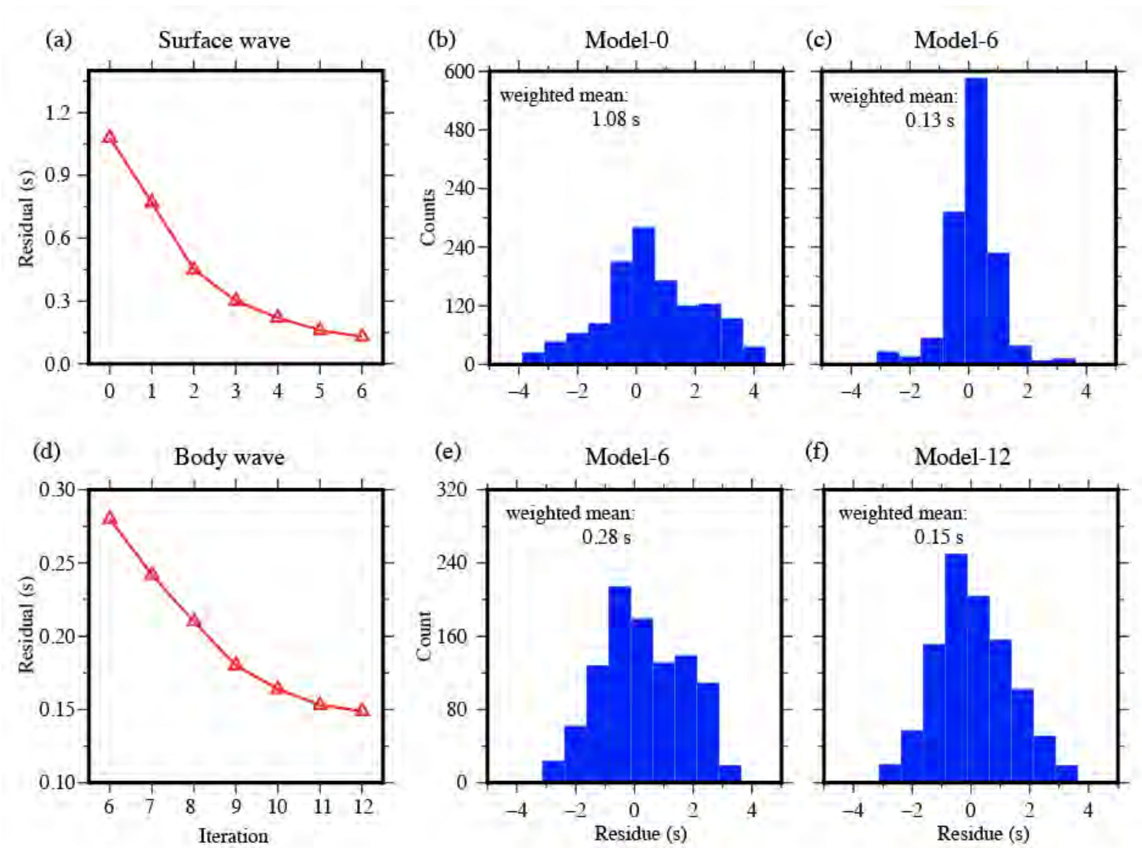

Figure 6: (a) Mean misfit reduction over first six iterations. (b) and (c) Histograms of surface wave misfit for initial model and model-6. (d) Total misfit reduction over iteration six to twelve. (e) and (f) Histograms of body misfit distribution of model-6 and Model-12, respectively.

Figures 7 and S2 present horizontal cross-sections of the final regional Vp and Vs models. The results are consistent overall with those of other velocity models in this region (e.g., White et al. 2021; Tong et al. 2021; Fang et al. 2022), but with a higher resolution owing to the inclusion of high-frequency data recorded by dense 2D arrays. Figure S3 shows the differences between the final and initial Vs models. At shallow depth, the final velocity model is slightly slower than the initial model, which is consistent with the decreasing trend of the positive travel time residuals shown in Figure 6a and 6d. The most significant changes concentrate along the main fault zones in this region, with a velocity reduction up to 500 m/s along the Garlock Fault and the main ruptures of the Ridgecrest sequence. In the middle crust, the final model is almost identical to the initial model with Vs difference less than 100 m/s, indicating that the initial middle crust model is fairly good. As the regional model at the middle crust is already systematically discussed in previous studies, we describe results of the regional model with a focus on the uppermost crust where we have significant improvements.

The study region is situated in the southern part of the Basin and Range province, characterized by alternating basins (or valleys) and mountains. As depicted in the geological map (Figure S4), the basins are predominantly covered by alluvium and sandstones at shallow depths, while the mountains are primarily composed of granodiorite and basalt. In the shallow crust, at depths less than 3.0 km, the most pronounced and lowest Vp and Vs anomalies are identified in the Indian Wells Valley (Figs. 7a-c and 7e-g) in agreement with the P wave travel time tomography results of Tong et al. (2021). The shape of these low-velocity anomalies in our model corresponds well with the inferred shape of the basin based on the surface geology. Low velocities and high Vp/Vs ratios (>1.8) may indicate that the unconsolidated alluvium and sandstones in the IWV basin extend to a depth of 4 km. The Vs in the IWV is slightly slower than surrounding areas to depths of up to 6 km (Figure S2b-c). However, the Vp/Vs ratios at this depth range tend to be normal (~1.76; Fig. S2j-k). This low Vs may be associated with the consolidated sedimentary rocks highly compacted by strata pressures. Furthermore, we observe similar low-velocity and high Vp/Vs features (Vp<5.1 km/s, Vs<3.0 km/s, and Vp/Vs >1.8) in other prominent valleys in the region (Figure 7a-b), such as the Searles Valley, Fremont Valley, and Panamint Valley. Conversely, high-velocity anomalies at shallow depths are predominantly associated with the mountains, including the Sierra Nevada and Argus Mountains. Generally, these valleys and mountains exhibit strong correlations with the low and high-velocity anomalies in our model results.

At shallow depths, other prominent features include low Vs along the major fault and rupture zones. The left-lateral Garlock Fault, which is the second-largest fault in southern California, is imaged as a long zone with Vp/Vs anomaly to a depth of 4 km (Figure 7j-k and S3j). The low-velocity zones at the two ends of the Garlock Fault may be associated with the FV and SV basins, while the internal part of the low velocity zone may reflect damaged fault rocks producing perhaps together with fluids high Vp/Vs ratios. These features extend in the Vs and Vp/Vs results to a depth of 4 km but are not clear in the Vp model. Low Vs and high Vp/Vs anomalies with depths up to 4 km are also found in the orthogonal northwest-trending and northeast-trending main rupture zones of the 2019 Ridgecrest Sequence (Figures 7c,k). Some low Vs zones extend at some locations along the main rupture of the 2019 Ridgcrest sequence to a depth up to 6 km (Figures 7b-c and S2a-c). These relatively deep anomalies may be produced by a combination of the local geology (Figure S4), the principal stress directions (Yang & Hauksson 2013), and major fault stepovers (Finzi et al., 2009).

In the middle crust, one of the most prominent features is the low Vp and low Vs velocity zones with a standard Vp/Vs surrounding the northern part of the Coso Volcanic and geothermal field (Figure 7d). This is consistent with the P- and S-wave travel time tomography results of Zhang & Lin (2014). The Coso geothermal field (CGF) is located between the Sierra Nevada batholith and the Basin and Range Province in Southeastern California (Figure 1). As one of the largest geothermal fields in the US, it has been used to generate power through over 100 production wells since 1987 (Adams et al., 2000). The maximum heat flow of the geothermal field was estimated to be 10 times the background value of the Basin and Range (Combs, 1980). A crustal magma has been assumed to provide the primary heat source for the present surface geothermal system (Combs, 1980; Bacon et al., 1980; Duffield et al., 1980). Coso is in a trans-tensional tectonic regime, and the extension facilitates the ascent of magma.

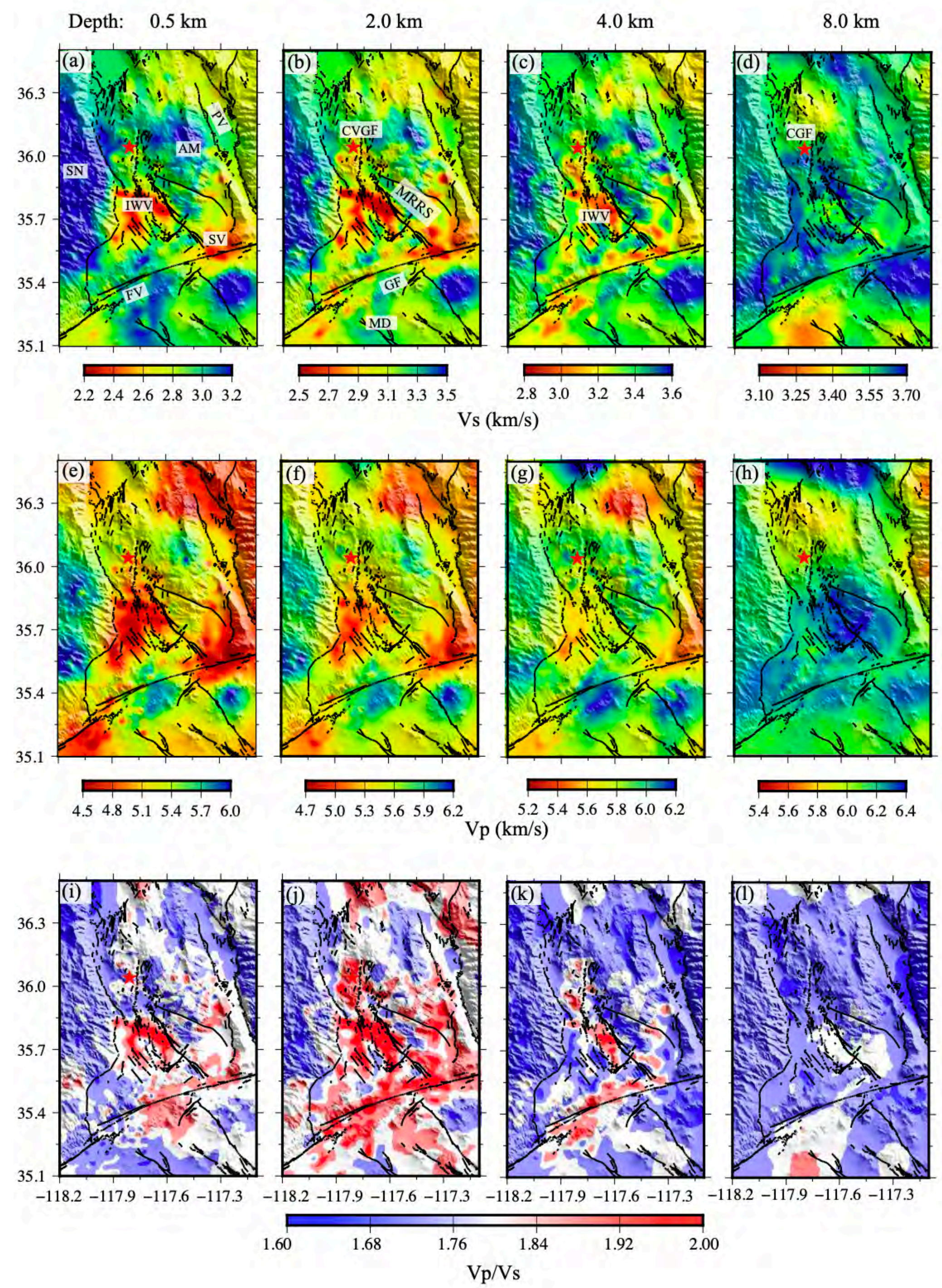

Figure 7: Map views of the regional velocity model at different depths. (a)-(d) S-wave (Vs) horizontal cross-sections at four different depths. (e)-(h) and (i)-(l) are similar to (a)-(d), but for P-wave (Vp) and Vp/Vs horizontal cross-sections, respectively. Major geological provinces in this region are labeled with abbreviations, including the Indian Wells Valley (IWV), Searles Valley (SV), Fremont Valley (FV), Panamint Valley (PV), Garlock Fault (GF), Main Ruptures of the 2019 Ridgecrest Sequence (MRRS), Mojave Desert (MD), Sierra Nevada (SN), Argus Mountains (AM) and the Coso Geothermal Field (CGF).

4.2 Fault zone models

Figures 8a and 8b illustrate the improvements in body wave fitting and source locations through the further development of fault zone models. As seen, the travel-time residual of both P and S waves decreases after the 7th iteration by up to 95% to 0.10 s and the location variations of relocated events stabilize. Consequently, the iterative updates to the model and event locations provide self-consistent velocity model and event positions. Figures 8c-8d further illustrate the residual distributions of regional Model-12 and the final fault zone model beneath the B4 array. For the regional Model-12, a positive residual persists, indicating that the regional model remains slightly faster than the crust beneath the B4 array. As demonstrated in Figure 9, the fault zone structure emerges within the regional model and includes additional high-resolution information on the velocities in the shallow crust and around the fault.

Figure 10 summarizes the derived Vs (top panels), Vp (middle panels) and Vp/Vs ratios (bottom panels) under the four linear arrays. Nearby events with a distance of less than 2.0 km to the linear arrays and magnitudes greater than 1.0 are projected onto the bottom panels and shown as black dots. The dashed white lines represent the location of mapped surface ruptures intersecting the linear arrays. The B1 array was located on the northern side and close to the epicenter of the Mw7.1 Ridgecrest event (Figure 1b). The results below B1 show a clear contrast of seismic velocities across the Mw7.1 rupture zone below 3 km, with a lower velocity in the southwest, along with flower-type low velocities in the top 3 km (Figure 10a-b) and anomalous Vp/Vs ratios that extend below the surface trace to about 6 km (Figure 10c). The velocity contrast at seismogenic depth is consistent with our regional velocity model (Figures 7a-c and e-g) and results from analyzing fault zone head and trapped waves (Qiu et al., 2021).

The B2 and B3 arrays were located close to the epicenter of the *M*6.4 event and primarily sampled the eastern part of the *M*7.1 rupture zone (Figure 1b) where granodiorite dominates the surface rocks (Figure S4). The primary characteristics of the velocity structure beneath the B2-B3 arrays are low Vs and high Vp/Vs anomalies, with core regions that are about 1 km wide located beneath the mapped surface ruptures (Figures 10d,f and g,i). These low Vs zones correlate with fault-damaged zones consistent with previous findings (Qiu et al., 2021). The Vp profiles exhibit approximately uniform low-velocity zones in the top 3 km, while the Vp/Vs ratios exhibit localized anomalies around the surface traces.

The B4 array was located in the southeast end of the *M*7.1 rupture zone, where it bifurcated into two sub-parallel strands, and close to the Garlock fault. At shallow depth, there is a low velocity layer with Vs less than 2.0 km/s and Vp/Vs greater than 2.1 (with largest values up to 3.0) that include localized zones with anomalous values below the surface rupture. The highly anomalous values layer in the top few hundred meters reflect the unconsolidated alluvium or sandstone at that location (Figure S4). Under the southwest strand of the mapped rupture, we imaged a low Vs anomaly with a width of ~1 km. The corresponding Vp/Vs anomaly extends to a depth of 5 km with a largest value of up to 2.0 at depths of 4.5-5.0 km. Under the west branch of the bifurcation, low Vs and high Vp/Vs zones extend to 3 km in depth. The estimated average width of this anomaly is up to 3.0 km, with a localized high Vp/Vs anomaly at about 5 km.

It is interesting to note that the seismicity (black dots) tends to concentrate around high Vp/Vs anomalies. At shallow depth (<2.0 km), multiple horsetail structures oriented obliquely to the main rupture are observed below all the arrays in the Vs maps, and in somewhat different forms also the Vp/Vs ratios (Fig. 10, top and bottom panels). These horsetail structures are consistent with fault geometries revealed by relocated seismicity (Ross et al., 2019). However, those features and the localized low velocity zones below surface traces are missing in the Vp images for arrays B1-B3 and exist only mildly below array B4 (Fig. 10, middle panels). This may be partially attributed to the lower resolution of Vp compared with Vs, since the wavelength of Vp is almost double that of Vs at the same period and may also reflect the fact that Vp reductions within the damaged fault zone rocks are smaller than the Vs reductions.

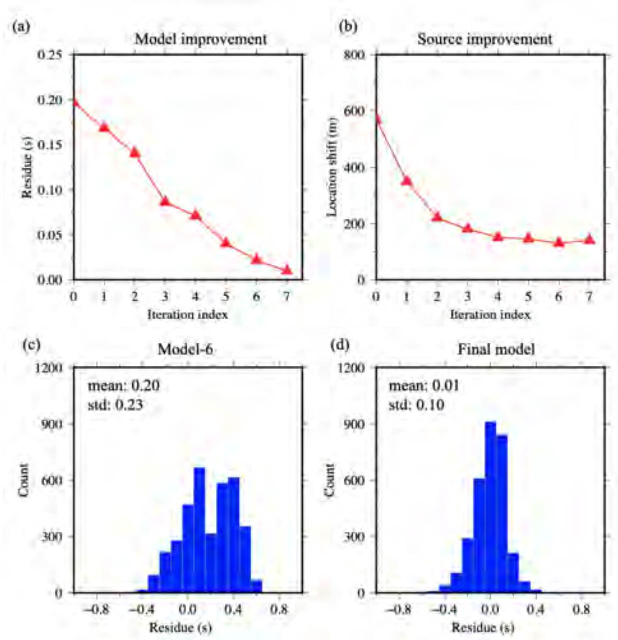

Figure 8: (a) Model misfit evolutions iterations. (b) Source location improvements over iterations. (b) and (c) Histograms of body wave travel time residuals for regional model and final fault zone models.

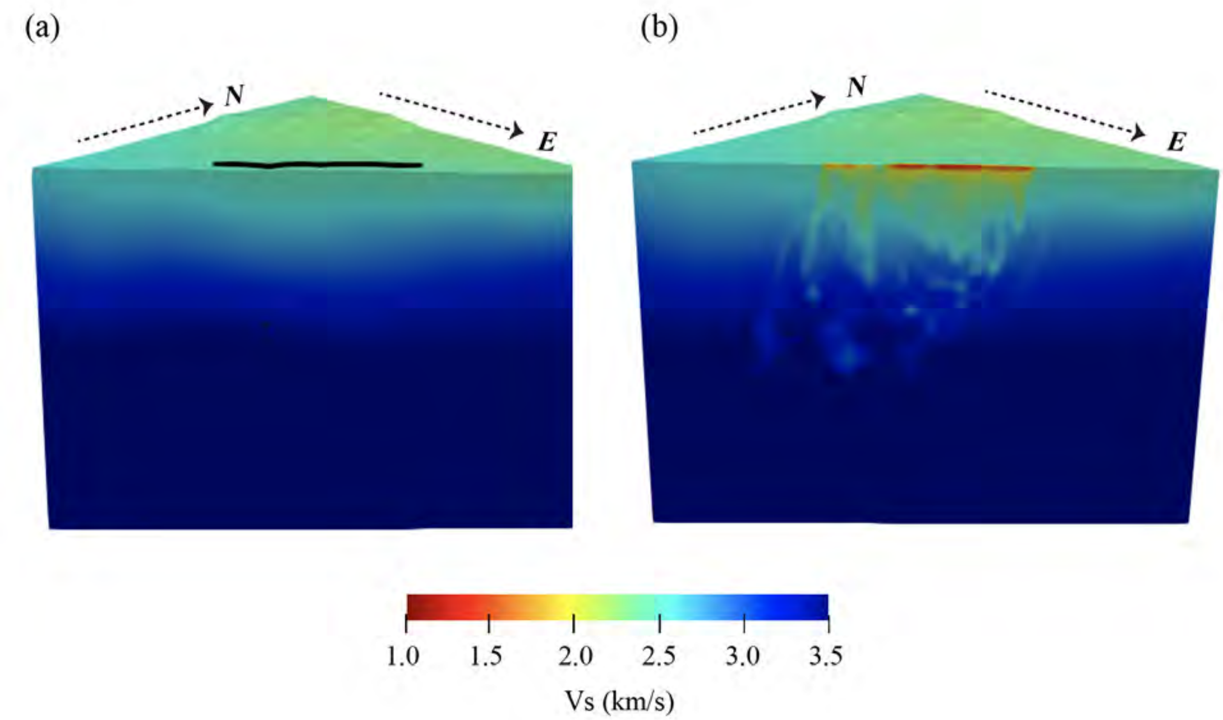

Figure 9: The initial (a) and finally inverted Vs model (b) under B4 array. The black symbols in (a) show the location of the B4 array.

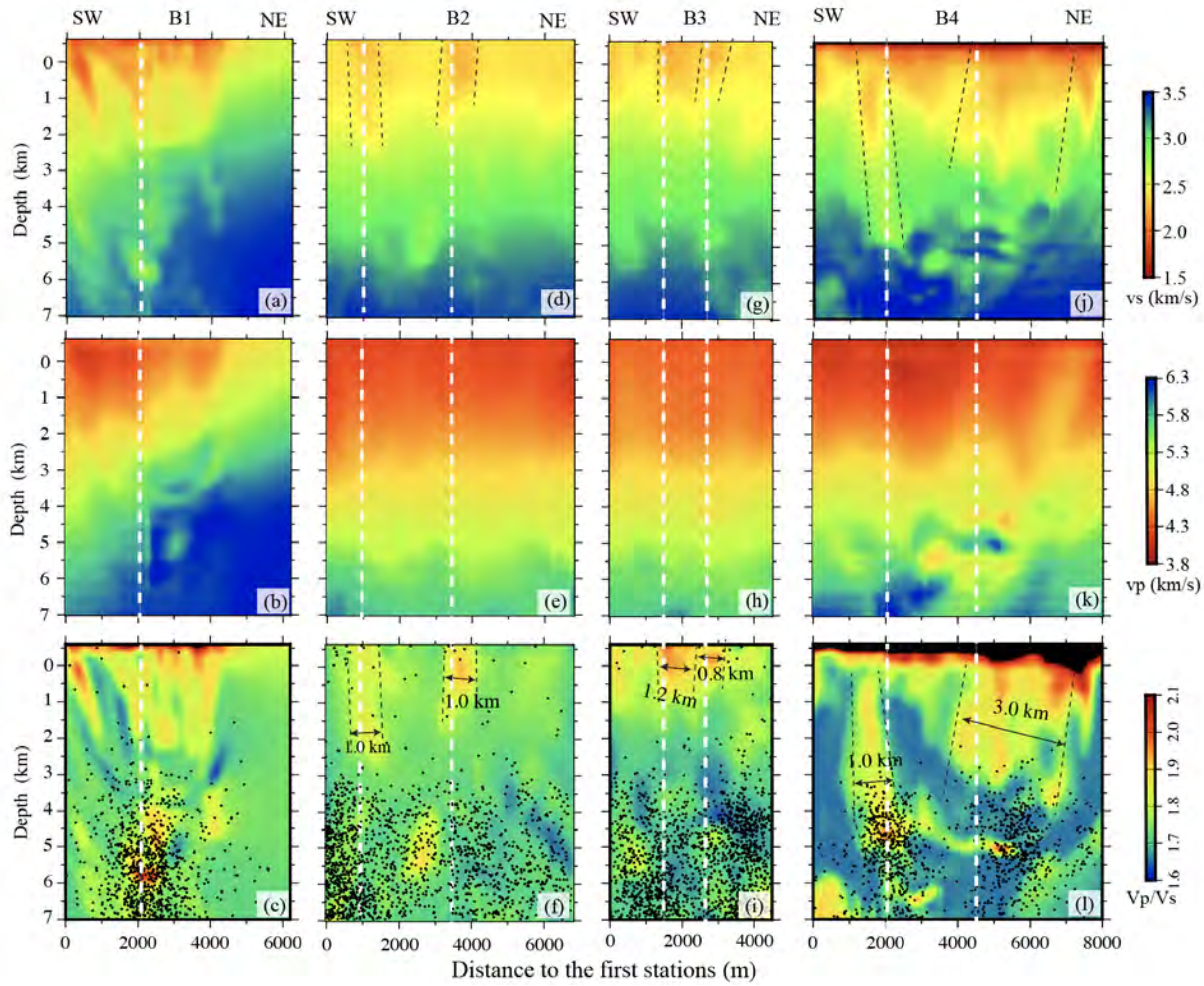

Figure 10: Panels (a) to (l) show the Vs, Vp, and Vp/Vs profiles under the B1-B4 arrays. The dashed white lines mark the locations of surface-mapped ruptures that intersect the linear arrays and the black lines mark locations of the low Vs and high Vp/Vs anomalies, with numbers denoting the estimated average widths. Events with distances less than 2.0 km from the linear arrays and magnitudes greater than 1.0 are projected onto the profiles as black dots.

5. Discussion and conclusions

Driven by the need to enhance large scale models with higher resolution local information, geophysical observation systems have evolved over the past decade from regional-scale networks into multiscale configurations. The region around Ridgecrest provides an excellent example for multi-scale seismic observations with high-density 2D and linear arrays deployed to complement the broader regional network. Multi-scale observations capture signals across a wide range of frequencies, which can be used to derive information (e.g., seismic velocity models) that cover multiple spatial dimensions and resolutions. Assimilating data from multi-scale networks consistently into one model is challenging using current inversion techniques (Fichtner et al., 2018). Consequently, previous seismic velocity models for the regional and fault zone scales in the Ridgecrest area (e.g., White et al., 2021; Qiu et al., 2021; Fang et al., 2022; Tong et al., 2021; Zhou et al., 2022; Qiu et al., 2023) were derived separately using either regional or dense array data, rendering them distinct and potentially incompatible with each other.

Previous fault-zone models have been primarily constructed by inverting noise-based correlation functions or by analyzing fault-zone related waves (e.g., Ben-Zion et al., 2003; Lin et al., 2013; Hillers et al., 2014; Roux et al., 2016; Wang et al., 2019; Catchings et al., 2020; Qiu et al., 2021). In the former approach, the depth of illumination is a quarter of the observational length due to the far-field approximation and the shallow sensitivity of surface waves. The far-field approximation necessitates that the extracted wavelengths of surface waves should be less than half of the array's aperture (e.g., Bensen et al., 2007; Luo et al., 2015). The shallow sensitivity of surface waves further restricts the optimal imaging depth to the upper half of the wavelength (e.g., Chong et al., 2014; Li et al., 2016). Consequently, noise-based inversion techniques have limited penetration into seismogenic depths. Analyzing fault zone head and trapped waves sensitive to bimaterial interfaces and damage zones (e.g. Ben-Zion and Aki, 1990; Peng et al., 2003) can circumvent these depth limitations, but this approach can only yield results for simplified tabular structures within homogeneous surrounding rocks, averaging over variations along strike and depth (e.g., Igel et al., 1997; Jahnke et al., 2002).

The existing models for the Ridgecrest region were constructed with various techniques not fully accounting for 3D wave propagation effects such as focusing, defocusing and wavefront healing effects. For instance, Tong et al. (2021) constructed P and S velocity models using the Ekonial tomography method and identified a significant Vp/Vs anomaly at depths ranging from 2-8 km, covering the area of the 2019 Ridgecrest rupture zones. Qiu et al. (2021) used travel time delays, amplification patterns, and waveform modeling of fault zone waves recorded by the dense linear arrays to image damage zones around the mainshock rupture, with significant reduction of S wave velocity and low attenuation coefficient in the top 3-5 km of the crust. Zhou et al. (2022) used noise-based cross-correlations and machine learning to develop an S wave velocity model for the Ridgecrest region that includes flower-shaped low velocity zones around the M6.4 and M7.1 ruptures.

To provide improved multi-scale Vp, Vs, and Vp/Vs velocity models for the Ridgecrest region, we developed and applied an iterative full waveform tomographic imaging method, using both regional and fault zone scale seismic data. Accurate source origin time, location, and focal mechanism are important for deriving reliable velocity models; the contributions of these source parameters and velocity models to the misfit are highly nonlinear and coupled. Our analysis includes relocating the 103 earthquakes used in the imaging process, during which the horizontal and vertical event locations shift on average by 500 m and 900 m, respectively. The final locations of these events are listed in the supplementary information. Potential errors of origin times and focal mechanisms can bias the derived models. The incorporation of double-difference kernels (Yuan et al., 2016; Chen et al., 2023) in full waveform inversion may help to overcome these problems and improve future multiscale tomographic imaging.

The derived Vp and Vs regional models provide improved background frameworks for embedding the higher-resolution information on internal properties of the rupture zones and the top crust. The regional models show low Vs and high Vp/Vs anomalies along the Garlock Fault and the rupture zones of the main 2019 Ridgecrest earthquakes (Fig. 7). The fault-zone models reveal further narrow zones with prominent low Vs and high Vp/Vs beneath the surface-mapped rupture zones (Fig. 10). In contrast, the Vp models do not show low-velocity rocks along the main fault and rupture zones in both the regional and fault-scale models. This may be partially attributed to the lower resolution of P-wave data, but can also reflect the fact that the S velocity and Vp/Vs ratio (or Poisson's ratio) are more strongly affected by the high crack density in damage rocks than P waves (e.g., Mavko et al., 1998; Hamiel et al., 2004). The presence of fluids in damaged rocks amplifies the differences between the reduction of S and P wave velocities (Brocher, 2005). High Vp/Vs ratios can also reflect bulk chemical composition such as anorthosite-rich metamorphic rocks (e.g., Christensen 1996; Brocher 2005), but this does not explain the concentration of high Vp/Vs ratios in our results around the fault and rupture zone structures.

To highlight additional structural details, Figures 11 and S5 display derived seismic velocities along vertical cross sections that cross the rupture zone of the M7.1 mainshock at various locations (see Figure 1b). The four vertical profiles in Figure 11 illustrate structures associated from northwest to southeast with the northern rupture terminus, the region around the M7.1 hypocenter, the rupture zone of the M6.4 event and its intersection with the rupture zone of the M7.1 mainshock, and the southern end of the Ridgecrest rupture zone near the Garlock fault. In addition to low velocities and high Vp/Vs anomalies in the shallow crust, the results for profiles 4-6 show high Vp/Vs anomalies below the rupture zone that coincide with (or flanked by) dense clusters of seismicity. The high high Vp/Vs anomaly and low Vs zone are especially pronounced at profile 5 which overlaps with the rupture zone of the M6.4 event, and to a lesser extent at profile 6 close to the southeast end of the M7.1 rupture. The seismicity in profile 3 near the northwest end of the mainshock rupture includes a horizontal branch to the northeast at depth of 3-5 km concluding with a zone of relatively low Vp/Vs ratio. Profiles 1 and 2 have high Vp/Vs anomalies close to the Coso geothermal region while the results for profile 7 include a shallow layer with low velocity Vp and Vs dipping to the northeast and lateral variations in the shallow Vp/Vs values (Figure S5). The hypocenters of the M6.4 and M7.1 events are located in zones with moderately low Vs values and high Vp/Vs ratios, but it is not clear if these structures existed before the events. The results are generally consistent with previous tomographic images in the area (e.g. Tong et al., 2021; While et al., 2021). Further interpretations of the velocities in terms of rock composition, crack density, and fluid content (e.g., Mavko et al. 1998; Brocher 2005) require more detailed local information not currently available.

Figure 12 shows the contrast of shear wave velocities across the Garlock Fault in the study area. The presented Vs contrast is the ratio of the average Vs values within 20 km south of the fault divided by the corresponding values north of the fault. Corresponding plots based on velocities averaged within 10 km, 5 km and 1 km from the Garlock fault show essentially the same results in somewhat more patchy forms for smaller crustal volumes (Fig. S6). The results exhibit clear velocity contrasts everywhere across the fault, with some polarity reversals both along strike and with depth. The polarity reversals along strike reflect changes in the rock bodies that are in contact along the fault, and are seen at different scales in other large structures including the San Andreas fault near Parkfield (Eberhart-Phillips & Michael, 1993; Thurber et al., 2006) and around the San Gorgonio Pass (Fang et al., 2016; Share & Ben-Zion, 2016), the San Jacinto fault (Allam et al., 2014), and sections of the north Anatolian fault (Dor et al., 2008; Ozakin et al., 2012). To the west of ~117.5 degrees longitude, the contrast at seismogenic depth with lower velocities south of the Garlock fault is consistent with results of Qiu et al. (2023) based on fault zone head waves generated by aftershocks at that fault section. The reversal of velocity contrast at shallow depth likely reflects different sedimentary covers across the fault. The velocity contrasts at different sections of the Garlock fault can affect directivities of earthquake ruptures and generation of rock damage asymmetry at these sections (e.g., Andrews & Ben-Zion, 1998; Ben-Zion & Shi, 2005; Shlomai & Fineberg, 2016), along with derived earthquake locations and focal mechanisms (e.g., McNally & McEvilly, 1977; McGuire & Ben-Zion, 2005). The reversal of the velocity contrast along strike can produce strong dynamic changes of normal stress that may aid or impede continuing earthquake ruptures depending on the propagation direction and velocity (e.g., Weertman, 1980; Ben-Zion, 2001; Shlomai et al., 2020).

The refined Vp and Vs models obtained in this study can be used to improve derivations of earthquake source properties (e.g., Takemura et al., 2018; Wang & Zhan, 2020; Simutė et al., 2023), and to conduct simulations of dynamic ruptures and earthquake ground motion (e.g., Thakur et al., 2020; Abdelmeguid & Elbanna, 2022; Taufiqurrahman et al., 2023; Yeh & Olsen, 2023) that account for the damage structures around the M6.4 and M7.1 events and low velocities in the shallow crust. The developed methodology can be used to perform similar multi-scale tomographic imaging at locations (e.g., the San Jacinto fault zone, the Parkfield section of the San Andreas fault) with dense arrays of sensors embedded in regional seismic networks. Updating in the derivation also the origin times and focal mechanisms of earthquakes used in the analysis will improve the results. Some such studies will be the subject of follow up research.

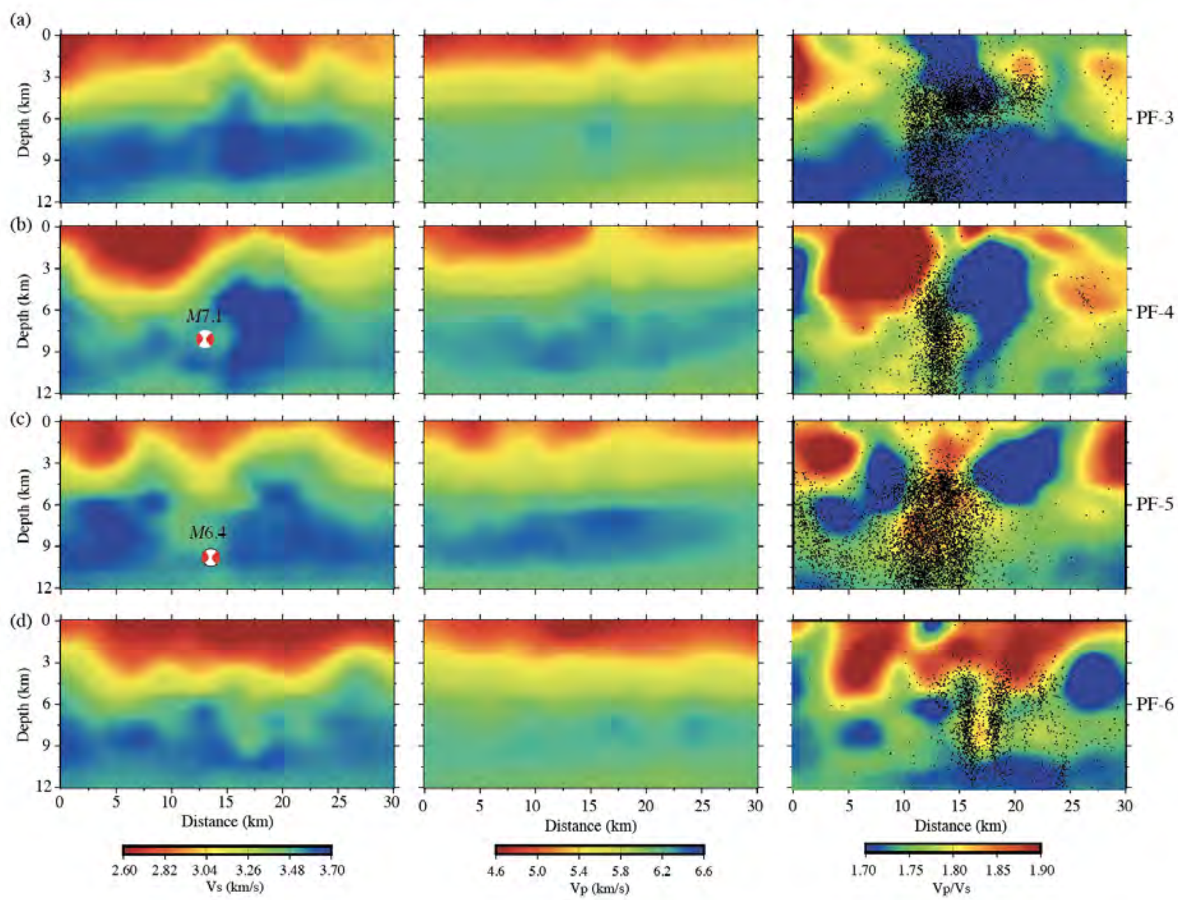

Figure 11: Panels (a) to (d) show cross-sections of Vs, Vp, and Vp/Vs profiles at the locations marked in Figure 1b. The rupture zone of the M7.1 Ridgecrest mainshock is centered at a horizontal distance of 15 and beach balls show the hypocenter and focal mechanisms of the M7.1 and M6.4 events. Aftershocks within 5.0 km from the cross-sections and with magnitudes greater than 1.0 are projected onto the Vp/Vs profiles as black dots.

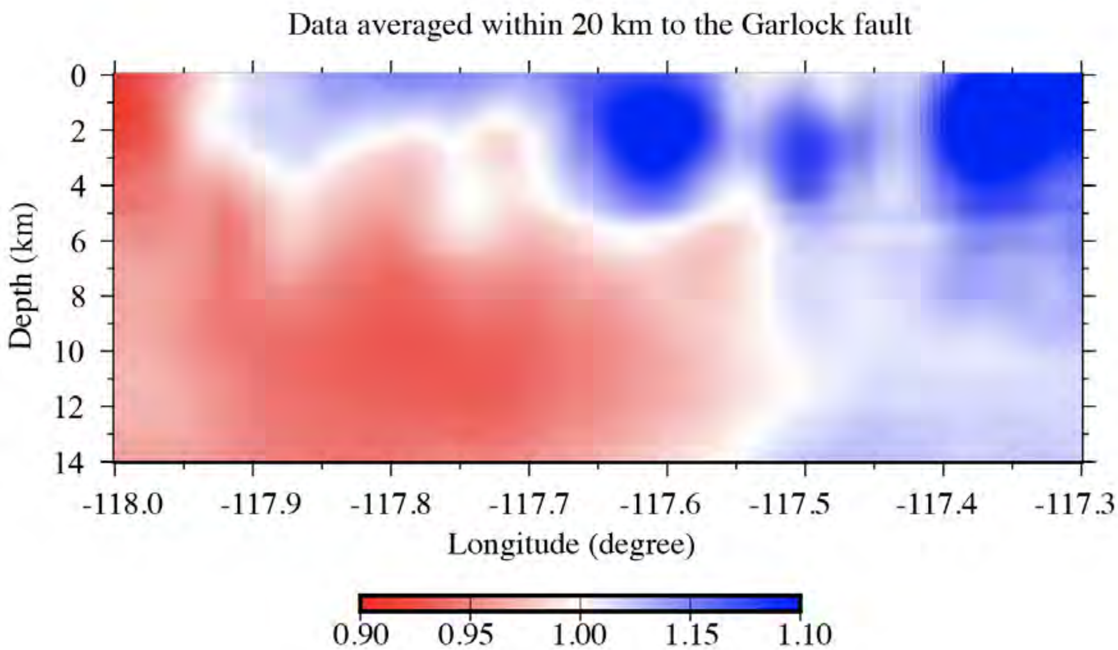

Figure 12: Ratios of Vs in the crustal block south of the Garlock fault in the study area divided by Vs north of the fault.

Acknowledgments

We thank Shuye Huang and Hongrui Qiu for help with data organization. The study was supported by the Statewide California Earthquake Center based on Award DE-SC0016520 from the U. S. Department of Energy. This work used the Expanse supercomputer (NSF award# 1928224) at the San Diego Supercomputer Center (SDSC) through an allocation from the Advanced Cyberinfrastructure Coordination Ecosystem: Services & Support (ACCESS) program, which is supported by National Science Foundation grants #2138259, #2138286, #2138307, #2137603, and #2138296.

Data Availability

The continuously recorded data used in the study are accessible through the Incorporated Research Institutions for Seismology Data Management Center (https://ds.iris.edu/ds/nodes/dmc/). The employed initial velocity models and earthquake catalog can be obtained from the supplementary materials of Fang et al. (2022, https://data.mendeley.com/datasets/4rdhjsc54p/1) and White et al. (2021, https://data.mendeley.com/datasets/x8v5wkbj6r/3), respectively. The derived Vp and Vs velocity models can be obtained from https://drive.google.com/drive/u/0/folders/1TVdnzM7E0--LSaC9TUEqdq_cCLEEKnjs.

References:

Abdelmeguid, M., & Elbanna, A. (2022). Sequences of seismic and aseismic slip on bimaterial faults show dominant rupture asymmetry and potential for elevated seismic hazard. *Earth and Planetary Science Letters*, 593, 117648. https://doi.org/10.1016/j.epsl.2022.117648.

Adams, M., J. Moore, S. Bjornstad, and D. Norman (2000), Geologic history of the Coso geothermal system, Trans. *Geotherm. Resour. Counc.*, 24, 205–210.

Ajala, R., Persaud, P., Stock, J. M., Fuis, G. S., Hole, J. A., Goldman, M., & Scheirer, D. (2019). Three-dimensional basin and fault structure from a detailed seismic velocity model of Coachella Valley, Southern California. Journal of Geophysical Research: Solid Earth, 124, 4728–4750. https://doi.org/10.1029/2018JB016260

Ajala, R., & Persaud, P. (2021). Effect of merging multiscale models on seismic wavefield predictions near the southern San Andreas fault. Journal of Geophysical Research: Solid Earth, 126, e2021JB021915.

Aki, K. & Richards, P. G. Quantitative Seismology 2nd edn (University Science Books, 2022).

Allam, A., Ben-Zion, Y., Kurzon, I., & Vernon, F. (2014). Seismic velocity structure in the Hot Springs and Trifurcation areas of the San Jacinto fault zone, California, from double-difference tomography. Geophysical Journal International, 198(2), 978–999. https://doi.org/10.1093/gji/ ggu176

Andrews, D. J., & Ben-Zion, Y. (1997). Wrinkle-like slip pulse on a fault between different materials. Journal of Geophysical Research, 102(B1), 553–571. https://doi.org/10.1029/96jb02856.

Bacon, C., W. Duffield, and K. Nakamura (1980), Distribution of Quaternary rhyolite domes of the Coso range, California: Implications for extent of the geothermal anomaly, J. Geophys. Res., 85(B5), 2425–2433.

Ben-Zion, Y. (2001). Dynamic ruptures in recent models of earthquake faults, J. Mech. Phys. Solids 49, 2209–2244.

Ben-Zion, Y. (2008). Collective Behavior of Earthquakes and Faults: Continuum-Discrete Transitions, Evolutionary Changes and Corresponding Dynamic Regimes, Rev. Geophysics, 46, RG4006, doi:10.1029/2008RG000260.

Ben-Zion, Y. and Aki, K. (1990). Seismic radiation from an SH line source in a laterally heterogeneous planar fault zone, Bull. Seism. Soc. Am., 80, 971-994.

Ben-Zion, Y., Z. Peng, D. Okaya, L. Seeber, J. G. Armbruster, et al., (2003). A shallow fault zone structure illuminated by trapped waves in the Karadere-Duzce branch of the North Anatolian Fault, western Turkey, *Geophys. J. Int.*, 152, 699-717.

Ben-Zion, Y., & Shi, Z. (2005). Dynamic rupture on a material interface with spontaneous generation of plastic strain in the bulk. Earth and Planetary Science Letters, 236(1–2), 486–496. https://doi.org/10.1016/j.epsl.2005.03.025.

Bensen, G. D., Ritzwoller, M. H., Barmin, M. P., Levshin, A. L., Lin F., Moschetti, M. P., et al. (2007), Processing seismic ambient noise data to obtain reliable broad-band surface wave dispersion measurements, Geophys. J. Int., 169(3), 1239–1260.

Brocher, T. M. (2005). Compressional and shear wave velocity versus depth in the San Francisco bay area, California: Rules for USGS Bay Area velocity model 05.0.0, U.S. Geol. Surv. Tech. Rept. OFR-2005-1317, available at http://pubs.usgs.gov/of/2005/1317/ (last accessed August 2012).

Callaghan, S., Maechling, P. J., Silva, F., Milner, K. R., Olsen, K. B., Graves, R. W. (2023). Recent Enhancements to the CyberShake PSHA Platform, Poster Presentation at 2023 SCEC Annual Meeting.

Catchings, R. D., Goldman, M.R., Steidl, J.H., Chan, et al. (2020). Nodal Seismograph Recordings of the 2019 Ridgecrest Earthquake Sequence, Seism. Res. Lett., 91, 3622–3633, doi: 10.1785/0220200203.

Catchings, R. D., Rymer, M. J., Goldman, M. R. (2020). San Andreas Fault Exploration Using Refraction Tomography and S-Wave-Type and Fault Mode Guided Waves, Bull. Seismol. Soc. Am. XX, 1–15, doi: 10.1785/0120200136.

Chen, G., Chen, J., Tape, C., Wu, H.,& Tong, P. (2023). Double-difference adjoint tomography of the crust and uppermost mantle beneath Alaska. Journal of Geophysical Research: Solid Earth, 128, e2022JB025168. https://doi.org/10.1029/2022JB025168

Cheng, Y., Hauksson, E., & Ben-Zion, Y. (2023). Refined earthquake focal mechanism catalog for southern California derived with deep learning algorithms. Journal of Geophysical Research: Solid Earth, 128, e2022JB025975.

Chong, J., Ni, S., Zhao, L. (2014), Joint inversion of crustal structure with the Rayleigh wave phase velocity dispersion and the ZH ratio, Pure Appl. Geophys., doi:10.1007/s00024-014-0902-z.

Christensen, N. I. (1996). Poisson's ratio and crustal seismology. Journal of Geophysical Research, 101(B2), 3139–3156.

Combs, J. (1980). Heat flow in the Coso geothermal area, Inyo County, California, J. Geophys. Res., 85(B5), 2411–2424.

Dor, O., Yildirim, C., Rockwell, T. K., Ben-Zion, Y., et al. (2008). Geologic and geomorphologic asymmetry across the rupture zones of the 1943 and 1944 earthquakes on the North Anatolian Fault: Possible signals for preferred earthquake propagation direction, Geophys. J. Int., 173, 483–504, doi:10.1111/j.1365-246X.2008.03709.x.

Duffield, W., C. Bacon, and G. Dalrymple (1980), Late Cenozoic volcanism, geochronology, and structure of the Coso Range, Inyo County, California, J. Geophys. Res., 85(B5), 2381–2404.

Eberhart-Phillips, D. & Michael, A.J. (1993). Three-dimensional velocity structure, seismicity, and fault structure in the Parkfield region, central California, J. Geophys. Res., 98, 15,737–15,758.

Fang, H., White, M. C. A., Lu, Y., & Ben-Zion, Y. (2022). Seismic traveltime tomography of Southern California using Poisson-Voronoi cells and 20 years of data. Journal of Geophysical Research: Solid Earth, 127, e2021JB023307. https:// doi.org/10.1029/2021JB023307.

Fang, H., Zhang, H., Yao, H., Allam, A., Zigone, D., et al. (2016), A new three-dimensional joint inversion algorithm of body-wave and surface-wave data and its application to the Southern California Plate Boundary Region, J. Geophys. Res. Solid Earth, 121, 3557–3569, doi:10.1002/2015JB012702.

Fichtner A., Bunge H. P., and Igel H. (2006). The adjoint method in seismology: II. Applications: Traveltimes and sensitivity functionals, Phys. Earth planet. In., 157,105–123.

Fichtner, A., van Herwaarden, D.-P., Afanasiev, M., Simutė, S., Krischer, L., Çubuk-Sabuncu, Y., et al. (2018). The Collaborative Seismic Earth Model: Generation 1. Geophysical Research Letters, 45, 4007–4016.

Finzi, Y., Hearn, E. H., Ben-Zion, Y., Lyakhovsky, V. (2009). Structural properties and deformation patterns of evolving strike-slip faults: Numerical simulations incorporating damage rheology, Pure Appl. Geophys., 166, 1537–1573, doi: 10.1007/s00024-009-0522-1.

Graves, R.W. (1996). Simulating seismic wave propagation in 3D elastic media using staggered-grid finite diferences, Bull. seism. Soc. Am., 86, 1091-1106.

Hamiel, Y., Liu, Y., Lyakhovsky, V., Ben-Zion, Y., & Lockner, D. (2004). A visco-elastic damage model with applications to stable and unstable fracturing. Geophysical Journal International, 159, 1155–1165. https://doi.org/10.1111/j.1365-246X. 2004.02452.x.

Hillers, G., Campillo, M., Ben-Zion, Y., Roux, P. (2014). Seismic fault zone trapped noise, J. Geophys. Res., 119, doi:10.1002/2014JB011217.

Igel, H., Ben-Zion, Y., Leary, P. (1997). Simulation of SH and P-SV Wave Propagation in Fault Zones, Geophys. J. Int., 128, 533-546.

Jahnke, G., Igel, H., Ben-Zion, Y. (2002). Three-dimensional calculations of fault-zone-guided waves in various irregular structures, Geophys. J. Int., 151, 416-426.

Juarez, A., Ben-Zion, Y. (2020). Effects of Shallow-Velocity Reductions on 3D Propagation of Seismic Waves. Seismological Research Letters. 91 (6): 3313–3322.

Kim, Y., Liu, Q., Tromp, J. (2011). Adjoint centroid-moment tensor inversions, Geophys. J. Int., 186(1), 264–278.

Komatitsch, D. & Tromp, J. (1999). Introduction to the spectral element method for three-dimensional seismic wave propagation, Geophys. J. Int., 139, 806–822.

Lee, E., Chen, P., Jordan, T. H., Maechling, P. B., Denolle, M. A., & Beroza, G. C. (2014). Full-3-D tomography for crustal structure in South- ern California based on the scattering-integral and the adjoint-wavefield methods. Journal of Geophysical Research: Solid Earth, 119(8), 6421–6451. https://doi.org/10.1002/2014JB011346.

Li, G., H. Chen, F. Niu, Z. Guo, Y. Yang, and J. Xie (2016), Measurement of Rayleigh wave ellipticity and its application to the joint inversion of high-resolution S wave velocity structure beneath northeast China, J. Geophys. Res. Solid Earth, 121,864–880, doi:10.1002/2015JB012459.

Li, G., Niu, F., Yang, Y., & Xie, J. (2018). An investigation of time-frequency domain phase weighted stacking and its application to phase-velocity extraction from ambient noise's empirical Green's functions. Geophysical Journal International, 212, 1143–1156. https://doi.org/10.1093/gji/ggx448

Li, G., Tao, K., Chen, M., Li, J., Maguire R., Ma, X. (2022). Cartesian Meshing Spherical Earth (CMSE): A Code Package to Incorporate the Spherical Earth in SPECFEM3D Cartesian Simulations. Seismological Research Letters. 93 (2A): 986–996. doi: https://doi.org/10.1785/0220210131

Li, G., Yang, Y., Niu, F., & Chen, M. (2021). 3-D sedimentary structures beneath southeastern Australia constrained by passive seismic array data. Journal of Geophysical Research: Solid Earth, 126, e2020JB019998.

Lin, F., Li, D., Clayton, R., & Hollis, D. (2013). High-resolution 3D shallow crustal structure in Long Beach, California: Application of ambient noise tomography on a dense seismic array. Geophysics, 78(4), Q45–Q56. https://doi.org/10.1190/geo2012-0453.1

Liu, Q. & Tromp, J. (2006). Finite-frequency kernels based upon adjoint methods, Bull. seism. Soc. Am., 96, 2383–2397.

Lu, Y., Ben-Zion, Y. (2022). Validation of seismic velocity models in southern California with full-waveform simulations, Geophysical Journal International, 229-2, 1232–1254, https://doi.org/10.1093/gji/ggab534

Luo, Y., Yang, Y., Xu, Y., Xu, H., Zhao, K., Wang, K. (2015). On the limitations of interstation distances in ambient noise tomography, Geophysical Journal International, 201(2), P652–661, https://doi.org/10.1093/gji/ggv043

Mavko, G., Mukerji, T., & Dvorkin, J. (1998). The rock physics handbook: Tools for seismic analysis in porous media (p. 329).Cambridge: Cambridge University Press.

McGuire, J. and Ben-Zion, Y. (2005). High-resolution imaging of the Bear Valley section of the San Andreas Fault at seismogenic depths with fault-zone head waves and relocated seismicity, Geophys. J. Int., 163, 152-164, doi: 10.1111/j.1365-246X.2005.02703.x.

McNally, K.C. & McEvilly, T.V. (1977). Velocity contrast across the San Andreas Fault in central California, small-scale variations from P-wave nodal plane distortion, Bull. seism. Soc. Am., 67, 1565–1576.

Mordret, A., Roux, P., Boué, P., & Ben-Zion, Y. (2019). Shallow three-dimensional structure of the San Jacinto fault zone revealed from ambient noise imaging with a dense seismic array. Geophysical Journal International, 216(2), 896–905. https://doi.org/10.1093/gji/ggy464

Olsen, K. B., Day, S. M., Bradley, C. R. (2003). Estimation of Q for long- period (>2 sec) waves in the Los Angeles basins, Bull. Seismol. Soc. Am., 93, no. 2, 627–638, doi: 10.1785/0120020135.

Ozakin, Y., Ben-Zion, Y., Aktar, M., Karabulut, H., Peng, Z. (2012). Velocity contrast across the 1944 rupture zone of the North Anatolian fault east of Ismetpasa from analysis of teleseismic arrivals, Geophys. Res. Lett., 39, L08307, doi:10.1029/2012GL051426.

Peng, Z., Ben-Zion, Y., Michael, A. J., and Zhu, L. (2003). Quantitative analysis of seismic trapped waves in the rupture zone of the 1992 Landers, California earthquake: Evidence for a shallow trapping structure, Geophys. J. Int., 155, 1021-1041.

Qiu, H., Ben-Zion, Y., Catchings, R., Goldman, M. R., Allam, A. A., & Steidl, J. (2021). Seismic imaging of the Mw 7.1 Ridgecrest earthquake rupture zone from data recorded by dense linear arrays. Journal of Geophysical Research: Solid Earth, 126, e2021JB022043. https://doi.org/10.1029/2021JB022043

Qiu, H., Chi, B., & Ben-Zion, Y. (2023). Internal structure of the central Garlock fault zone from Ridgecrest aftershocks recorded by dense linear seismic arrays. Geophysical Research Letters, 50, e2022GL101761. https://doi. org/10.1029/2022GL101761.

Robertsson, J.O.A., 1996. A numerical free-surface condition for elastic/viscoelastic finite difference modeling in the presence of topography, Geophysics, 61, 1921-1934.

Ross, Z. E., Idini, B., Jia, Z., Stephenson, O. L., Zhong, M., Wang, X., et al. (2019). Hierarchical interlocked orthogonal faulting in the 2019 Ridgecrest earthquake sequence. Science, 366, 346–351.

Roux, P., Moreau, L., Lecointre, A., Hillers, G., Campillo, M., et al. (2016). A methodological approach toward high-resolution surface wave imaging of the San Jacinto Fault Zone using ambient-noise recordings at a spatially dense array, Geophys. J. Int., 206, 980–992, doi:10.1093/gji/ggw193.

Schliwa, N., Gabriel, A., & Ben-Zion, Y. (2023). 3D modeling of near-field ground motions and deformation in dynamic rupture simulations of the 2019 Ridgecrest earthquake including fault zone and fault roughness effects. Poster Presentation at 2023 SCEC Annual Meeting.

Shapiro, N.M., Campillo, M., Stehly, L. & Ritzwoller, M.H., 2005. High- resolution surface wave tomography from ambient seismic noise, Science, 307, 1615–1618.

Share, P.-E. & Ben-Zion, Y. (2016), Bimaterial interfaces in the south San Andreas Fault with opposite velocity contrasts NW and SE from San Gorgonio Pass, Geophys. Res. Lett., 43, doi:10.1002/2016GL070774.

Shaw, J. H., Plesch, A., Tape, C., Suess, P. M., Jordan, T. H., Ely, G., et al. (2015). Unified structural representation of the southern California crust and upper mantle. Earth and Planetary Science Letters, 415, 1–15. https://doi.org/10.1016/j.epsl.2015.01.016

Shlomai, H., & Fineberg, J. (2016). The structure of slip-pulses and supershear ruptures driving slip in bimaterial friction. Nature Communications, 7(1), 11787. https://doi.org/10.1038/ncomms11787.

Simutė, S., Boehm, C., Krischer, L., Gokhberg, A., Vallée, M., & Fichtner, A. (2023). Bayesian seismic source inversion with a 3-D Earth model of the Japanese islands. Journal of Geophysical Research: Solid Earth, 128, e2022JB024231.

Takemura S., Shiomi K., Kimura T., Saito T., 2016. Systematic difference between first-motion and waveform-inversion solutions for shallow offshore earthquakes due to a low-angle dipping slab, Earth, Planets Space, 68, 149.10.1186/s40623-016-0527-9

Tao, K., Grand, S. P., & Niu, F. (2018). Seismic structure of the upper mantle beneath eastern Asia from full waveform seismic tomography. Geochemistry, Geophysics, Geosystems, 19. https://doi.org/10.1029/2018GC007460

Tarantola, A. (1984). Inversion of seismic reflection data in the acoustic ap- proximation, Geophysics, 49, 1259–1266.

Taufiqurrahman, T., Gabriel, A.-A., Li, D., Ulrich, T., Li, B., Carena, S., et al. (2013). Dynamics, interactions and delays of the 2019 Ridgecrest rupture sequence. Nature.,618, 308–315 (2023).

Thakur, P., Huang, Y., & Kaneko, Y. (2020). Effects of low-velocity fault damage zones on long-term earthquake behaviors on mature strike slip faults. Journal of Geophysical Research: Solid Earth, 125(8), e2020JB019587. https://doi.org/10.1029/2020JB019587

Thurber, C.H., Zhang, H., Waldhauser, F., Hardebeck, J., Michael, A. & Eberhart-Phillips, D. (2006). Three-dimensional compressional wave speed model, earthquake relocations, and focal mechanisms for the Parkfield, California, region, Bull. Seismol. Soc. Am., 96(4B), S38-S49, doi: 10.1785/0120050825.

Tong, P., Yao, J., Liu, Q., Li, T., Wang, K., Liu, S., et al. (2021). Crustal rotation and fluids: Factors for the 2019 Ridgecrest earthquake sequence? Geophysical Research Letters, 48, e2020GL090853. https://doi.org/10.1029/2020GL090853

Tromp, J. Tape, C., and Liu, Q. (2005). Seismic tomography, adjoint methods, time reversal and banana-doughnut kernels, Geophys. J. Int., 160, 195–216.

Wang, X., & Zhan, Z. (2020). Moving from 1-D to 3-D velocity model: Automated waveform-based earthquake moment tensor inversion in the Los Angeles region. Geophysical Journal International, 220(1), 218–234. https://doi.org/10.1093/gji/ggz435.

Wang, Y., Allam, A., & Lin, F.-C. (2019). Imaging the Fault Damage Zone of the San Jacinto Fault Near Anza With Ambient Noise Tomography Using a Dense Nodal Array. Geophysical Research Letters, 46,12,938–12,948.

Warner, M., Ratcliffe, A., Nangoo, T., Morgan, J., Umpleby, A., Shah, N., et al. (2013). Anisotropic 3D full-waveform inversion. Geophysics, 78(2), R59–R80.

Weertman, J. (1980). The stopping of a rising liquid-filled crack in the Earth's crust by a freely slipping horizontal joint. Journal of Geophysical Research, 85, 967–976.

White, M. C. A., Fang, H., Catchings, R. D., et al. (2021). Detailed traveltime tomography and seismic catalogue around the 2019 Mw7.1 Ridgecrest, California, earthquake using dense rapid-response seismic data, Geophysical Journal International, vol. 227, no. 1, pp. 204-227.

Yang, W. & Hauksson, E. (2013). The tectonic crustal stress field and style of faulting along the Pacific North America Plate boundary in Southern California. Geophys. J. Int., 194, 100–117.

Yeh, T.-Y., and K. B. Olsen (2023). Fault Damage Zone Effects on Ground Motions during the 2019 Mw 7.1 Ridgecrest, California, Earthquake, Bull. Seismol. Soc. Am. XX, 1–15, doi: 10.1785/0120220249.

Yuan, Y., Simons, F. & Tromp, J. (2016). Double-difference adjoint seismic tomography. Geophys. J. Int. 206, 1599–1618.

Zhang, Q. & Lin, G. (2014). Three-dimensional Vp and Vp/Vs models in the Coso geothermal area, California: Seismic character- ization of the magmatic system, J. Geophys. Res., 119, 4907–4922, doi:10.1002/2014JB010992.

Zhou, Z., Bianco, M., Gerstoft, P., Olsen, K. (2022). High-resolution imaging of complex shallow fault zones along the July 2019 Ridgecrest ruptures, Geophys. Res. Lett., 49, no. 1, e2021GL095024.

Zigone, D., Ben-Zion, Y., Lehujeur, M., Campillo, M., Hillers, G., & Vernon, F. L. (2019). Imaging subsurface structures in the San Jacinto fault zone with high-frequency noise recorded by dense linear arrays. Geophysical Journal International, 217(2), 879–893. https://doi.org/10.1093/gji/ggz069.

JGR: Solid Earth

Supporting Information for

Multi-scale seismic imaging of the Ridgecrest, CA, region with full-waveform inversions of regional and dense array data

Guoliang Li[1*], Yehuda Ben-Zion[1]

[1] Department of Earth Sciences and Statewide California Earthquake Center, University of Southern California, Los Angeles, CA, USA

* Correspondence to: Guoliang Li, guoleonlee@gmail.com

Introduction

This file contains two tables, two explanatory texts, and six additional figures for the results presented in the main manuscript:

Table S1: 29 Earthquake information used in updating regional scale model. That information includes the origin times, locations, relocations, magnitudes, and focal mechanisms.

Table S2: Events used for building fault-zone scale models. That information includes the origin times, locations, relocations, magnitudes, and focal mechanisms.

Text S1: Definition of the weights used in the adjoint tomography.

Text S2: Derivations of using the adjoint method to calculate the gradients of model parameters and source parameters.

Figure S1: The mesh for the volumes around array B1, B2-B3 arrays.

Figure S2: Horizontal cross-sections of the final regional models at depths of 3 km, 5 km, 6 km, and 7 km.

Figure S3: Model comparisons between the final inverted and initial regional models.

Figure S4: Geological map of surface rock types in the study region.

Figure S5: Vertical sections of Vs, Vp and Vp/Vs profiles crossing the main rupture zones of the 2019 Ridgecrest Earthquakes.

Figure S6: Vs contrast along Garlock Fault calculated from results within 2 km, 5 km and 10 km to the Garlock Fault.

Table S1: 29 Earthquakes used in updating regional scale model.

Origin time (CMT)	Original location	Relocated	Magnitude	Focal mechanisms
2019-07-17T10:48:29.644	(36.1481, -117.9351, 3.51)	(36.1465,-117.9266, 2.32)	2.08	(135.0, 90.0, 174.0)
2019-07-10T00:16:30.347	(35.3570, -117.9324, 2.58)	(35.3569,-117.9326, 1.77)	2.71	(117.0, 89.0, -92.0)
2019-07-14T12:29:33.350	(35.3320, -117.9119, 8.59)	(35.3342,-117.9112, 8.57)	3.09	(3.0, 38.0, -84.0)
2019-07-08T03:15:14.661	(35.3819, -117.8487, 3.16)	(35.3848,-117.8494, 3.19)	2.70	(319.0, 75.0,-169.0)
2019-07-07T14:46:40.182	(35.9145, -117.7100, 2.07)	(35.9123,-117.7193, 1.28)	3.54	(162.0, 86.0,-157.0)
2019-07-07T15:48:10.581	(35.8303, -117.6296,19.15)	(35.8298,-117.6289,18.36)	3.63	(68.0, 33.0, 19.0)
2019-07-07T21:02:51.155	(35.7838, -117.6000,12.92)	(35.7769,-117.5976,11.69)	3.48	(170.0, 57.0,-153.0)
2019-07-07T14:14:15.761	(35.6914, -117.5420,12.61)	(35.6910,-117.5393,11.44)	2.70	(180.0, 39.0,-125.0)
2019-07-07T14:21:35.049	(35.6437, -117.4537, 5.74)	(35.6438,-117.4536, 5.15)	3.43	(325.0, 12.0, 169.0)
2019-07-16T11:50:02.440	(36.0125, -117.4022, 3.70)	(36.0098,-117.3911, 2.40)	2.55	(329.0, 14.0,-133.0)
2019-07-15T12:42:31.770	(36.0742, -117.3842, 3.12)	(36.0740,-117.3854, 2.27)	2.00	(281.0, 66.0,-176.0)
2019-07-11T06:03:11.911	(36.0398, -117.3543, 3.20)	(36.0407,-117.3578, 2.39)	2.61	(148.0, 64.0,-180.0)
2019-07-11T05:43:35.658	(36.0570, -117.3432, 4.46)	(36.0571,-117.3434, 3.81)	3.05	(302.0, 75.0, 159.0)
2019-07-16T00:26:09.156	(36.0347, -117.3181, 2.64)	(36.0350,-117.3182, 2.21)	2.64	(359.0, 26.0, -66.0)
2019-07-08T22:18:48.921	(35.9332, -117.3113, 7.16)	(35.9336,-117.3120, 6.21)	3.10	(300.0, 75.0,-146.0)
2019-07-08T17:53:46.717	(35.5491, -117.3085,10.59)	(35.5579,-117.3187, 9.13)	4.04	(308.0, 74.0, 160.0)
2019-07-08T04:59:53.748	(35.9729, -117.2933, 0.60)	(35.9730,-117.2913, 0.67)	2.98	(326.0, 86.0, 172.0)
2019-07-10T23:35:43.129	(35.9682, -117.2730, 5.20)	(35.9732,-117.2678, 4.70)	3.12	(156.0, 76.0, 157.0)
2019-07-23T12:03:42.489	(35.3818, -117.2362, 3.42)	(35.3750,-117.2362, 2.79)	2.65	(158.0, 80.0, 179.0)
2019-07-07T12:21:38.387	(35.6792, -117.4884, 5.00)	(35.6792,-117.4890, 4.04)	2.74	(289.0, 83.0, 95.0)
2019-07-07T13:13:13.701	(35.8811, -117.6869, 5.90)	(35.8811,-117.6868, 5.27)	2.82	(345.0, 83.0,-166.0)
2019-07-07T13:23:51.731	(35.9007, -117.6952, 3.26)	(35.8980,-117.6878, 2.75)	3.24	(344.0, 63.0,-155.0)
2019-07-07T15:00:03.950	(35.6310, -117.4256, 5.71)	(35.6319,-117.4243, 4.77)	2.39	(316.0, 88.0, 172.0)
2019-07-07T15:05:05.013	(35.5921, -117.4687, 2.79)	(35.5905,-117.4676, 1.08)	2.96	(146.0, 75.0, 163.0)
2019-07-07T18:40:35.380	(36.0982, -117.8384, 2.80)	(36.0989,-117.8405, 1.01)	2.78	(140.0, 87.0,-161.0)
2019-07-07T20:46:38.870	(35.7872, -117.4351,22.51)	(35.7865,-117.4378,21.64)	3.20	(195.0, 58.0,-150.0)
2019-07-08T00:16:07.992	(35.5698, -117.3578, 7.73)	(35.5669,-117.3615, 6.99)	2.74	(355.0, 85.0, 172.0)
2019-07-09T11:39:21.124	(36.1120, -117.5362, 3.18)	(36.1137,-117.5398, 0.95)	2.49	(309.0, 80.0, 168.0)
2019-07-10T01:58:59.881	(35.3924, -117.9411, 8.99)	(35.3920,-117.9413, 8.15)	3.12	(163.0, 72.0,-107.0)

Table S2: Events used for building fault-zone scale models.

(1) 20 events under B1 arrays

Origin time (CMT)	Original location	Relocated	Magnitude	Focal mechanisms
2019-07-15T02:08:54.600	(35.7826, -117.6009, 7.66)	(35.7835,-117.6001, 6.90)	1.79	(283.0, 82.0, 158.0)
2019-07-14T20:41:56.683	(35.7695, -117.5870, 8.17)	(35.7670,-117.5881, 6.88)	1.81	(261.0, 87.0,-126.0)
2019-08-02T14:18:53.761	(35.7630, -117.5890,11.93)	(35.7631,-117.5894,11.35)	1.83	(233.0, 42.0, -42.0)
2019-07-13T21:54:08.196	(35.7673, -117.5885, 4.49)	(35.7677,-117.5907, 4.36)	1.89	(71.0, 11.0, 47.0)
2019-07-13T07:46:55.528	(35.7887, -117.6085, 6.85)	(35.7877,-117.6079, 6.68)	1.90	(116.0, 88.0,-150.0)
2019-07-17T23:50:48.855	(35.7884, -117.6015, 4.47)	(35.7879,-117.5998, 4.29)	1.98	(158.0, 87.0, 129.0)
2019-07-16T04:11:07.337	(35.7750, -117.5927, 7.41)	(35.7741,-117.5947, 7.30)	2.00	(45.0, 33.0, -24.0)
2019-07-13T17:07:00.188	(35.7694, -117.5807, 9.38)	(35.7685,-117.5791, 8.05)	2.02	(126.0, 83.0, 153.0)
2019-07-15T06:38:25.507	(35.7674, -117.5869, 6.31)	(35.7689,-117.5920, 6.71)	2.04	(306.0, 90.0,-170.0)
2019-07-19T06:13:18.125	(35.7711, -117.5759,10.91)	(35.7712,-117.5777,11.03)	2.07	(310.0, 89.0,-149.0)
2019-07-30T05:19:02.749	(35.7829, -117.5871, 7.01)	(35.7841,-117.5877, 7.53)	2.08	(97.0, 81.0, 145.0)
2019-07-16T00:48:51.274	(35.7683, -117.5884,10.77)	(35.7678,-117.5901,10.36)	2.13	(174.0, 56.0,-176.0)
2019-07-14T02:32:41.724	(35.7840, -117.5937, 4.01)	(35.7837,-117.5928, 4.25)	2.20	(74.0, 78.0,-134.0)
2019-07-14T16:38:52.352	(35.7834, -117.5744, 6.20)	(35.7850,-117.5744, 6.18)	2.33	(122.0, 83.0, 101.0)
2019-07-20T09:58:13.440	(35.7971, -117.5912, 7.43)	(35.8004,-117.5834, 8.84)	2.41	(93.0, 42.0, -96.0)
2019-07-14T15:39:21.700	(35.7736, -117.5951, 4.62)	(35.7739,-117.5963, 4.38)	2.42	(156.0, 77.0,-155.0)
2019-07-19T02:05:12.516	(35.7837, -117.6184,10.89)	(35.7792,-117.6193,11.50)	2.45	(203.0, 41.0, -88.0)
2019-07-16T22:38:43.294	(35.7779, -117.5828, 4.40)	(35.7789,-117.5832, 4.15)	2.66	(286.0, 83.0, 166.0)
2019-07-14T11:46:10.986	(35.7844, -117.6161, 7.38)	(35.7794,-117.6147, 8.28)	2.78	(155.0, 42.0, 107.0)
2019-07-13T06:24:44.775	(35.7862, -117.5677,12.03)	(35.7880,-117.5643,12.60)	2.90	(320.0, 65.0,-154.0)

(2) 30 events under B2-B3 arrays

Origin time (CMT)	Original location	Relocated	Magnitude	Focal
2019-07-14T00:47:20.790	(35.6814, -117.5038,10.13)	(35.6791,-117.5014, 9.21)	2.38	(128.0, 86.0, 179.0)
2019-07-14T02:26:03.450	(35.6762, -117.5145, 5.62)	(35.6772,-117.5079, 4.98)	2.11	(345.0, 67.0,-167.0)
2019-07-15T04:01:50.625	(35.7025, -117.5103, 9.83)	(35.7025,-117.5107, 9.66)	2.20	(8.0, 60.0, 176.0)
2019-07-15T07:04:10.232	(35.6918, -117.5388,11.99)	(35.6925,-117.5389,11.69)	2.05	(130.0, 84.0, 170.0)
2019-07-15T08:10:58.597	(35.6723, -117.5085,10.64)	(35.6691,-117.5015, 9.59)	2.67	(118.0, 70.0,-146.0)
2019-07-15T10:29:10.398	(35.6846, -117.4766,10.04)	(35.6831,-117.4760, 9.67)	2.87	(339.0, 88.0, 173.0)
2019-07-16T04:44:58.659	(35.6980, -117.5230,11.20)	(35.6984,-117.5230,10.93)	2.05	(113.0, 79.0,-153.0)
2019-07-16T19:01:00.949	(35.6822, -117.5375, 6.10)	(35.6825,-117.5367, 6.27)	2.50	(185.0, 66.0,-105.0)
2019-07-17T02:20:21.161	(35.7077, -117.5012, 5.98)	(35.7077,-117.5008, 5.73)	2.15	(360.0, 53.0,-140.0)
2019-07-17T14:48:47.240	(35.6825, -117.4689, 6.91)	(35.6803,-117.4679, 6.56)	3.08	(346.0, 81.0,-177.0)
2019-07-18T00:38:15.402	(35.7132, -117.5075, 5.57)	(35.7130,-117.5058, 5.83)	2.06	(102.0, 87.0,-178.0)
2019-07-18T15:49:04.538	(35.7064, -117.5178,10.88)	(35.7064,-117.5194,10.13)	2.64	(335.0, 72.0,-171.0)
2019-07-18T15:55:16.702	(35.7131, -117.5081, 6.78)	(35.7132,-117.5043, 7.31)	2.33	(292.0, 41.0, -87.0)
2019-07-18T17:06:50.810	(35.6723, -117.5255, 7.39)	(35.6733,-117.5238, 6.89)	2.43	(353.0, 74.0,-165.0)
2019-07-18T19:27:45.980	(35.6922, -117.5192, 7.29)	(35.6939,-117.5205, 7.59)	2.45	(135.0, 48.0,-176.0)
2019-07-19T01:41:36.326	(35.6811, -117.4905, 5.92)	(35.6803,-117.4959, 6.35)	2.09	(312.0, 49.0,-141.0)
2019-07-19T13:42:39.812	(35.6712, -117.5300,11.09)	(35.6710,-117.5287,10.51)	2.03	(339.0, 73.0,-174.0)
2019-07-20T08:03:12.775	(35.6890, -117.5286, 8.21)	(35.6906,-117.5260, 8.09)	2.87	(115.0, 82.0, 167.0)
2019-07-20T08:53:45.670	(35.7022, -117.5450, 9.68)	(35.7007,-117.5439,10.03)	2.05	(125.0, 79.0,-153.0)
2019-07-21T03:35:14.305	(35.7071, -117.5382,11.36)	(35.7078,-117.5385,11.06)	2.34	(26.0, 71.0,-124.0)
2019-07-21T17:09:22.457	(35.6994, -117.5418,10.97)	(35.7010,-117.5411,10.55)	3.01	(153.0, 86.0, 173.0)
2019-07-22T18:29:17.804	(35.6941, -117.5082, 9.20)	(35.6938,-117.5088, 8.33)	2.06	(329.0, 52.0,-178.0)
2019-07-23T12:08:22.579	(35.6793, -117.5249,10.82)	(35.6786,-117.5256,11.13)	2.55	(4.0, 56.0,-123.0)
2019-07-23T16:45:57.985	(35.6658, -117.5035, 6.85)	(35.6665,-117.5045, 7.14)	2.13	(143.0, 29.0,-125.0)
2019-07-24T20:25:23.630	(35.6652, -117.5199,10.29)	(35.6652,-117.5203,10.35)	2.84	(14.0, 40.0, -93.0)
2019-07-30T15:39:19.605	(35.6817, -117.4902, 8.77)	(35.6823,-117.4906, 9.02)	2.36	(181.0, 56.0,-152.0)
2019-08-01T04:51:29.392	(35.7015, -117.4844, 7.44)	(35.7007,-117.4847, 7.24)	2.07	(83.0, 44.0, -24.0)
2019-08-01T11:04:15.632	(35.7273, -117.4721, 8.87)	(35.7261,-117.4732, 8.62)	2.77	(140.0, 76.0, 154.0)
2019-08-02T13:20:26.282	(35.7100, -117.5104, 8.88)	(35.7100,-117.5102, 8.93)	2.80	(293.0, 87.0,-177.0)
2019-08-08T01:13:17.949	(35.6852, -117.5487, 9.64)	(35.6858,-117.5483, 9.40)	2.10	(125.0, 76.0, 146.0)

(3) 24 events under B4 arrays

Origin time (CMT)	Original location	Relocated	Magnitude	Focal mechanisms
2019-07-16T08:42:28.560	(35.5509, -117.3843, 6.49)	(35.5509,-117.3847, 6.20)	2.66	(116.0, 83.0,-173.0)
2019-07-16T10:22:00.496	(35.5429, -117.4142, 6.31)	(35.5427,-117.4144, 6.14)	2.06	(289.0, 87.0, 126.0)
2019-07-16T10:52:32.763	(35.5955, -117.3730, 6.47)	(35.5955,-117.3733, 5.87)	3.48	(286.0, 81.0,-179.0)
2019-07-16T23:11:27.232	(35.5742, -117.3996, 5.98)	(35.5743,-117.3997, 5.75)	2.13	(2.0, 78.0,-169.0)
2019-07-17T14:42:44.190	(35.5647, -117.4065, 6.98)	(35.5638,-117.4061, 6.61)	2.01	(350.0, 78.0,-179.0)
2019-07-19T10:47:05.421	(35.5848, -117.3609, 5.55)	(35.5846,-117.3603, 5.34)	3.65	(133.0, 84.0, 178.0)
2019-07-19T11:04:06.429	(35.5864, -117.3626, 5.27)	(35.5856,-117.3623, 5.18)	2.07	(314.0, 88.0, 132.0)
2019-07-20T15:41:49.429	(35.5339, -117.3719, 9.54)	(35.5338,-117.3723, 8.91)	2.37	(344.0, 81.0,-177.0)
2019-07-21T14:54:52.166	(35.5710, -117.3580, 5.48)	(35.5710,-117.3581, 5.20)	2.16	(136.0, 69.0,-141.0)
2019-07-22T16:31:07.100	(35.5370, -117.3622, 9.74)	(35.5371,-117.3631, 9.20)	2.75	(155.0, 81.0,-179.0)
2019-07-22T23:18:41.787	(35.5669, -117.3939, 6.36)	(35.5656,-117.3931, 6.25)	2.21	(132.0, 72.0,-141.0)
2019-07-24T21:44:43.595	(35.5229, -117.4102, 8.50)	(35.5195,-117.4143, 8.33)	2.63	(151.0, 71.0, 176.0)
2019-07-26T01:18:03.396	(35.5534, -117.3777, 6.31)	(35.5535,-117.3781, 5.77)	2.59	(125.0, 84.0, 158.0)
2019-07-27T01:35:37.775	(35.5362, -117.3701,10.09)	(35.5361,-117.3700, 9.41)	3.56	(343.0, 82.0,-174.0)
2019-07-29T07:44:23.419	(35.5890, -117.3529, 5.79)	(35.5891,-117.3526, 5.49)	2.05	(102.0, 88.0,-120.0)
2019-07-29T13:33:40.843	(35.5333, -117.3717, 9.61)	(35.5333,-117.3696, 8.85)	2.03	(337.0, 89.0,-176.0)
2019-08-02T18:13:42.258	(35.5726, -117.3997, 6.17)	(35.5723,-117.3995, 5.84)	2.16	(285.0, 80.0, 169.0)
2019-08-05T21:19:12.415	(35.5712, -117.3834, 7.22)	(35.5711,-117.3837, 6.52)	2.25	(156.0, 80.0,-157.0)
2019-08-06T07:15:57.570	(35.5228, -117.4188, 9.57)	(35.5215,-117.4209, 9.13)	2.08	(149.0, 80.0,-179.0)
2019-08-06T10:42:12.296	(35.5540, -117.3553,10.21)	(35.5546,-117.3556, 9.71)	2.82	(148.0, 74.0,-176.0)
2019-08-06T11:25:17.820	(35.5543, -117.3555,10.29)	(35.5542,-117.3554, 9.61)	2.28	(138.0, 65.0, 151.0)
2019-08-06T12:03:25.691	(35.5433, -117.4064, 9.45)	(35.5418,-117.4088, 9.11)	2.21	(145.0, 82.0,-162.0)
2019-08-07T00:03:27.489	(35.5343, -117.3721, 9.49)	(35.5343,-117.3721, 8.84)	2.40	(159.0, 81.0, 177.0)
2019-08-08T08:25:38.836	(35.5178, -117.4214, 8.13)	(35.5180,-117.4212, 7.48)	2.14	(159.0, 86.0,-178.0)

Text S1: the total weighting term $w_{i,k}$ is determined by the waveform signal-to-noise ratio (SNR), waveform similarity and the cross-correlation time-shift (δt):

$$w_{i,k} = w_{snr} \times w_{cc} \times w_{\delta t},$$

where, w_{snr} is the weighting term related to the SNR of the observed waveforms with the following definition:

$$w_{snr} = \begin{cases} 1 & , \ snr \geq 7 \\ 0.5 + 0.5\cos\left(\frac{7-snr}{7-snr}\pi\right) & , 5 < snr < 7 \\ 0 & , \ snr \leq 5 \end{cases} .$$

The waveform similarity is defined as the maximum value of the normalized cross-correlation coefficient (CC) between the observed $u_{i,k}^{obs}(t)$ and synthetic $u_{i,k}^{syn}(t)$ waveforms between *i*th and *k*th source-receiver as:

$$cc = \max\left\{\frac{\int u_{i,k}^{obs}(t) \cdot u_{i,k}^{syn}(t-\tau)dt}{\sqrt{\int \left|u_{i,k}^{obs}(t)\right|^2 \cdot \left|u_{i,k}^{syn}(t)\right|^2 dt}}\right\},$$

and the corresponding weighting term w_{CC} is defined as:

$$w_{cc} = \begin{cases} 1 & , \ cc \geq 0.7 \\ 0.5 + 0.5\cos\left(\frac{0.7-cc}{0.7-0.5}\pi\right) & , 0.5 < cc < 0.7 \\ 0 & , \ cc \leq 0.5 \end{cases} .$$

The weighting term $w_{\delta t}$ is defined as:

$$w_{\delta t} = \begin{cases} 1 & , \ |\delta t| \leq 2 \\ 0.5 + 0.5\cos\left(\frac{2-|\delta t|}{3-2}\pi\right) & , 2 < |\delta t| < 3 \\ 0 & , \ |\delta t| \geq 3 \end{cases} .$$

Text S2: Derivations of the Adjoint method

The adjoint method is a mathematical tool that allows us to compute the gradient of an objective function with respect to the model and source parameters very efficiently. The derivations of the adjoint theory are well documented (e.g., Tarantola,1984; Tromp et al., 2005; Fichtner et al., 2006; Liu et al., 2006). In the following part we will follow the Liu et al. (2006) and derive a general formulation of the adjoint method that is used to calculate the gradients of velocity models and source parameters.

As shown in Tromp et al. (2005), one can choose to minimize any kinds of misfit functions, for example, cross-correlation based travel-time shift and normalized zero-lag cross-correlations. Different misfit functions simply give rise to different adjoint sources. For simplicity, we seek to minimize the least-square waveform misfit function:

$$\chi(s) = \frac{1}{2}\sum_{i=1}^{n}\int_{0}^{T}[\boldsymbol{d}(\boldsymbol{x_r}, t) - \boldsymbol{u}(\boldsymbol{x_r}, t)]^{2}\, dt \quad . \tag{1}$$

Synthetic waveform $\boldsymbol{u}(\boldsymbol{x_r}, t)$ at receiver location $\boldsymbol{x_r}$ with time an interval $[0, T]$ is subjected to wave equation:

$$\delta\rho\partial_t^2\boldsymbol{u} - \nabla\cdot\boldsymbol{T}{=}f \quad , \tag{2}$$

$\boldsymbol{d}(\boldsymbol{x_r}, t)$ denotes the observed data and ρ represent the distribution of density. $\boldsymbol{T}$ is related to the displacement gradient through Hooke's law:

$$\boldsymbol{T} = \boldsymbol{c}\colon\nabla\boldsymbol{u} \ , \tag{3}$$

where $\boldsymbol{c}$ denotes the elastic tensor. On the Earth's free surface $\partial\boldsymbol{G}$ the traction must vanish:

$$\boldsymbol{n}\cdot\boldsymbol{T} = 0 \tag{4}$$

In addition to the boundary condition, the waveform equation (2) also satisfies the initial conditions:

$$\boldsymbol{u}(\boldsymbol{x_r}, 0) = 0 \ \text{, and } \partial_t\boldsymbol{u}(\boldsymbol{x_r}, 0) = 0 \ . \tag{5}$$

In the case of a point source at location $\boldsymbol{x_s}$, it can be written in terms of the moment tensor $\boldsymbol{M}$ and source time function *S(t)*:

$$\boldsymbol{f}{=}{-}\boldsymbol{M}\cdot\nabla\delta(\boldsymbol{x} - \boldsymbol{x_s},)S(t) \tag{6}$$

The objective function (1) is constrained by wave equation (2); therefore, we can construct the Lagrange function:

$$\chi = \frac{1}{2}\sum_{i=1}^{n}\int_{0}^{T}[\boldsymbol{d}(\boldsymbol{x_r}, t) - \boldsymbol{u}(\boldsymbol{x_r}, t)]^{2}\, dt - \int_{0}^{T}\int_{\boldsymbol{G}}\lambda[\rho\partial_t^2\boldsymbol{u} - \nabla\cdot\boldsymbol{T} - \boldsymbol{f}]d^3x dt \ , \tag{7}$$

where, the Lagrange multiplier $\boldsymbol{\lambda}(\boldsymbol{x}, t)$ is undetermined. By perturbing the misfit χ we can obtain:

$$
\begin{aligned}
\delta\chi = &\int_0^T \int_{\boldsymbol{G}} \sum_r [\boldsymbol{u}(\boldsymbol{x_r}, t) - \boldsymbol{d}(\boldsymbol{x_r}, t)]\delta(\boldsymbol{x} - \boldsymbol{x_r})\delta\boldsymbol{u}(\boldsymbol{x_r}, t) d^3 x dt \\
&- \int_0^T \int_{\boldsymbol{G}} \boldsymbol{\lambda}[\rho\partial_t^2 \delta\boldsymbol{u} - \nabla \cdot (\boldsymbol{c}: \nabla\delta\boldsymbol{u})] d^3 x dt \\
&- \int_0^T \int_{\boldsymbol{G}} \lambda[\delta\rho\partial_t^2 \boldsymbol{u} - \nabla \cdot (\delta\boldsymbol{c}: \nabla\boldsymbol{u}) - \delta\boldsymbol{f}] d^3 x dt.
\end{aligned} \tag{8}
$$

As the initial conditions: $\boldsymbol{u}(\boldsymbol{x_r}, 0) = 0$ and $\partial_t \boldsymbol{u}(\boldsymbol{x_r}, 0) = 0$, the perturbation of the initial conditions are also zeros, that is, $\delta\boldsymbol{u}(\boldsymbol{x_r}, 0) = 0$ and $\partial_t \delta\boldsymbol{u}(\boldsymbol{x_r}, 0) = 0$. Similarly, the perturbation of boundary satisfies: $\boldsymbol{n} \cdot [\delta\boldsymbol{c}: \nabla\boldsymbol{u} + \boldsymbol{c}: \nabla\delta\boldsymbol{u}] = 0$. With the following three equivalent transformations:

$$
\begin{cases}
\boldsymbol{\lambda} \cdot \partial_t^2 \delta\boldsymbol{u} = [\boldsymbol{\lambda} \cdot \partial_t \delta\boldsymbol{u} - \partial_t \lambda \cdot \delta\boldsymbol{u}]_t' + \partial_t^2\, \boldsymbol{\lambda} \cdot \delta\boldsymbol{u} \\
\boldsymbol{\lambda} \cdot [\nabla \cdot (\delta\boldsymbol{c}: \nabla\boldsymbol{u})] = \nabla \cdot (\boldsymbol{\lambda} \cdot \delta\boldsymbol{c}: \nabla\boldsymbol{u}) - \nabla \cdot \boldsymbol{u}(\delta\boldsymbol{c}: \nabla\lambda) \\
\boldsymbol{\lambda} \cdot [\nabla \cdot (\boldsymbol{c}: \nabla\delta\boldsymbol{u})] = \nabla \cdot (\boldsymbol{\lambda} \cdot \boldsymbol{c}: \nabla\delta\boldsymbol{u}) - \nabla \cdot (\delta\boldsymbol{u} \cdot \boldsymbol{c}: \nabla\boldsymbol{\lambda}) + \delta\boldsymbol{u} \cdot [\nabla \cdot (\boldsymbol{c}: \nabla\boldsymbol{\lambda})]
\end{cases} \tag{9}
$$

the equation (8) can be further written as:

$$
\begin{aligned}
\delta\chi = &\int_0^T \int_{\boldsymbol{G}} \sum_r [\boldsymbol{u}(\boldsymbol{x_r}, t) - d(\boldsymbol{x_r}, t)]\delta(\boldsymbol{x} - \boldsymbol{x_r})\delta\boldsymbol{u}(\boldsymbol{x_r}, t) d^3 x dt \\
&- \int_0^T \int_{\boldsymbol{G}} [\delta\rho\boldsymbol{\lambda} \cdot \partial_t^2 \boldsymbol{u} - \nabla\boldsymbol{\lambda}: \delta\boldsymbol{c}: \nabla\boldsymbol{u} - \boldsymbol{\lambda} \cdot \delta\boldsymbol{f}] d^3 x dt \\
&- \int_0^T \int_{\boldsymbol{G}} [\rho\partial_t^2 \boldsymbol{\lambda} - \nabla \cdot (\boldsymbol{c}: \nabla\boldsymbol{\lambda})] \cdot \delta\boldsymbol{u} d^3 x dt \\
&- \int_{\boldsymbol{G}} \rho[\boldsymbol{\lambda} \cdot \partial_t \delta\boldsymbol{u} - \partial_t \boldsymbol{\lambda} \cdot \delta s]_T \cdot \delta\boldsymbol{u} d^3 x \\
&- \int_0^T \int_{\boldsymbol{G}} \boldsymbol{n} \cdot (\boldsymbol{c}: \nabla\boldsymbol{\lambda}) d^3 x dt
\end{aligned} \tag{10}
$$

Therefore, if the Lagrange multiplier $\boldsymbol{\lambda}(x,t)$ satisfies:

$$
\rho\partial_t^2 \boldsymbol{\lambda} - \nabla \cdot (\boldsymbol{c}: \nabla\boldsymbol{\lambda}) = \sum_{r=1}^n [\boldsymbol{d}(\boldsymbol{x_r}, t) - \boldsymbol{u}(\boldsymbol{x_r}, t)]\, \delta(\mathbf{x} - \boldsymbol{x_r}) \tag{11}
$$

and subjective to the free surface boundary condition:

$$
\boldsymbol{n} \cdot (\boldsymbol{c}: \nabla\boldsymbol{\lambda}) = 0 \quad , \tag{12}
$$

and the end condition:

$$
\boldsymbol{\lambda}(\boldsymbol{x_r}, T) = 0 \quad \text{and} \quad \partial_t \boldsymbol{\lambda}(\boldsymbol{x_r}, T) = 0 \quad , \tag{13}
$$

the perturbation of the $\delta\chi$ or equation (10) can be simplified as:

$$\delta\chi = \int_0^T \int_{\boldsymbol{G}} (\delta\rho\boldsymbol{\lambda}\cdot\partial_t^2\boldsymbol{u} + \nabla\boldsymbol{\lambda}:\delta\boldsymbol{c}:\nabla\boldsymbol{s} - \boldsymbol{\lambda}\cdot\delta\boldsymbol{f})d^3x dt \ . \tag{14}$$

Equation (14) tell us that the change in the misfit function $\delta\chi$ is determined by the model parameters $\delta\rho$, $\delta\boldsymbol{c}$ and source parameter $\delta\boldsymbol{f}$ in terms of the original wavefield $\boldsymbol{u}$ determined by equations (2)-(5) and the Lagrange multiplier wavefield $\boldsymbol{\lambda}$ determined by equations (11)-(13).

Let us define the adjoint wave field $\boldsymbol{u}^\dagger$ in terms of the Lagrange multiplier wavefield $\boldsymbol{\lambda}$ by:

$$\boldsymbol{u}^\dagger(\boldsymbol{x},t) = \boldsymbol{\lambda}(\boldsymbol{x},T-t) \tag{15}$$

That is, the adjoint wave field is the time-reversed Lagrange multiplier wavefield $\boldsymbol{\lambda}$. Then the adjoint wave field $\boldsymbol{u}^\dagger(\boldsymbol{x},t)$ is determined by the set of equations:

$$\rho\partial_t^2\boldsymbol{u}^\dagger - \nabla\cdot\left(\boldsymbol{c}:\nabla\boldsymbol{u}^\dagger\right) = \textstyle\sum_{r=1}^{n}[\boldsymbol{d}(\boldsymbol{x}_{\boldsymbol{r}},T-t) - \boldsymbol{u}(\boldsymbol{x}_{\boldsymbol{r}},T-t)]\,\delta(\mathbf{x}-\boldsymbol{x}_{\boldsymbol{r}}), \tag{16}$$

and is subject to the free surface boundary condition:

$$\boldsymbol{n}\cdot(\boldsymbol{c}:\nabla\boldsymbol{u}^\dagger) = 0 \ , \tag{17}$$

and the initial conditions:

$$\boldsymbol{u}^\dagger(\boldsymbol{x}_{\boldsymbol{r}},0) = 0 \quad \text{and} \quad \partial_t\boldsymbol{u}^\dagger(\boldsymbol{x}_{\boldsymbol{r}},0) = 0 \ . \tag{18}$$

Comparing equations (16)-(18) with (2)-(5), we can see that the adjoint wavefield $\boldsymbol{u}^\dagger(\boldsymbol{x}_{\boldsymbol{r}},t)$ satisfies the same wave equation, boundary condition and initial conditions, except for the source term. The adjoint wavefield is determined by the time-reversed difference between synthetics and observed waveforms.

Using the adjoint wavefield, the perturbation of the misfit function (14) can be expressed as:

$$\delta\chi = \int_{\boldsymbol{G}} \delta\rho K_\rho + \delta\boldsymbol{c} :: K_c d^3x + \int_0^T \int_{\boldsymbol{G}} \boldsymbol{u}^\dagger(\boldsymbol{x},T-t)\delta\boldsymbol{f} d^3x dt, \tag{19}$$

where the $K\rho$ and Kc are density and elastic tensor kernels and defined as:

$$\begin{cases} K_\rho = \int_0^T \boldsymbol{u}^\dagger(\boldsymbol{x},T-t)\cdot\partial_t^2\boldsymbol{u}(\boldsymbol{x},t)dt \\ Kc(x) = \int_0^T \nabla\boldsymbol{s}^\dagger(x,T-t)\cdot\nabla s(x,t)dt \end{cases} \tag{20}$$

The first order perturbation of the point source (equation 6) can be written as:

$$\delta\boldsymbol{f} = \delta\boldsymbol{M}\cdot\nabla\delta(\boldsymbol{x}-\boldsymbol{x}_s) + \boldsymbol{M}\cdot\nabla\nabla_S\delta(\boldsymbol{x}-\boldsymbol{x}_s)\cdot\delta\boldsymbol{x}_s + \boldsymbol{M}\cdot\nabla\delta(\boldsymbol{x}-\boldsymbol{x}_s)\delta S \ . \tag{21}$$

If we neglect the model variation, the source perturbations can be written as:

$$\delta\chi = \int_0^T \int_{\boldsymbol{G}} \boldsymbol{u}^\dagger(\boldsymbol{x},T-t)\cdot\{\delta\boldsymbol{M}\cdot\nabla\delta(\boldsymbol{x}-\boldsymbol{x}_s) + \boldsymbol{M}\cdot\nabla\nabla_S\delta(\boldsymbol{x}-\boldsymbol{x}_s)\cdot\delta\boldsymbol{x}_s + \boldsymbol{M}\cdot\nabla\delta(\boldsymbol{x}-\boldsymbol{x}_s)\delta S\}d^3x dt \tag{22}$$

Although the adjoint method can obtain the gradients of moment tensors, source locations and source time functions, only gradients of the source locations are used to do relocations. The moment tensor and source time function are fixed.

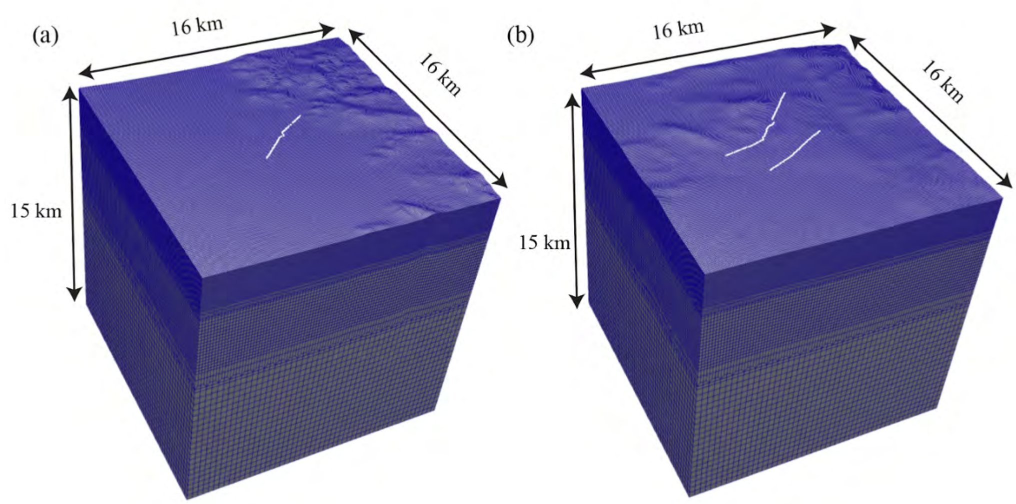

Figure S1: The mesh for the volumes around array B1 (a) and arrays B2-B3 (b) with white dots representing the locations of linear arrays.

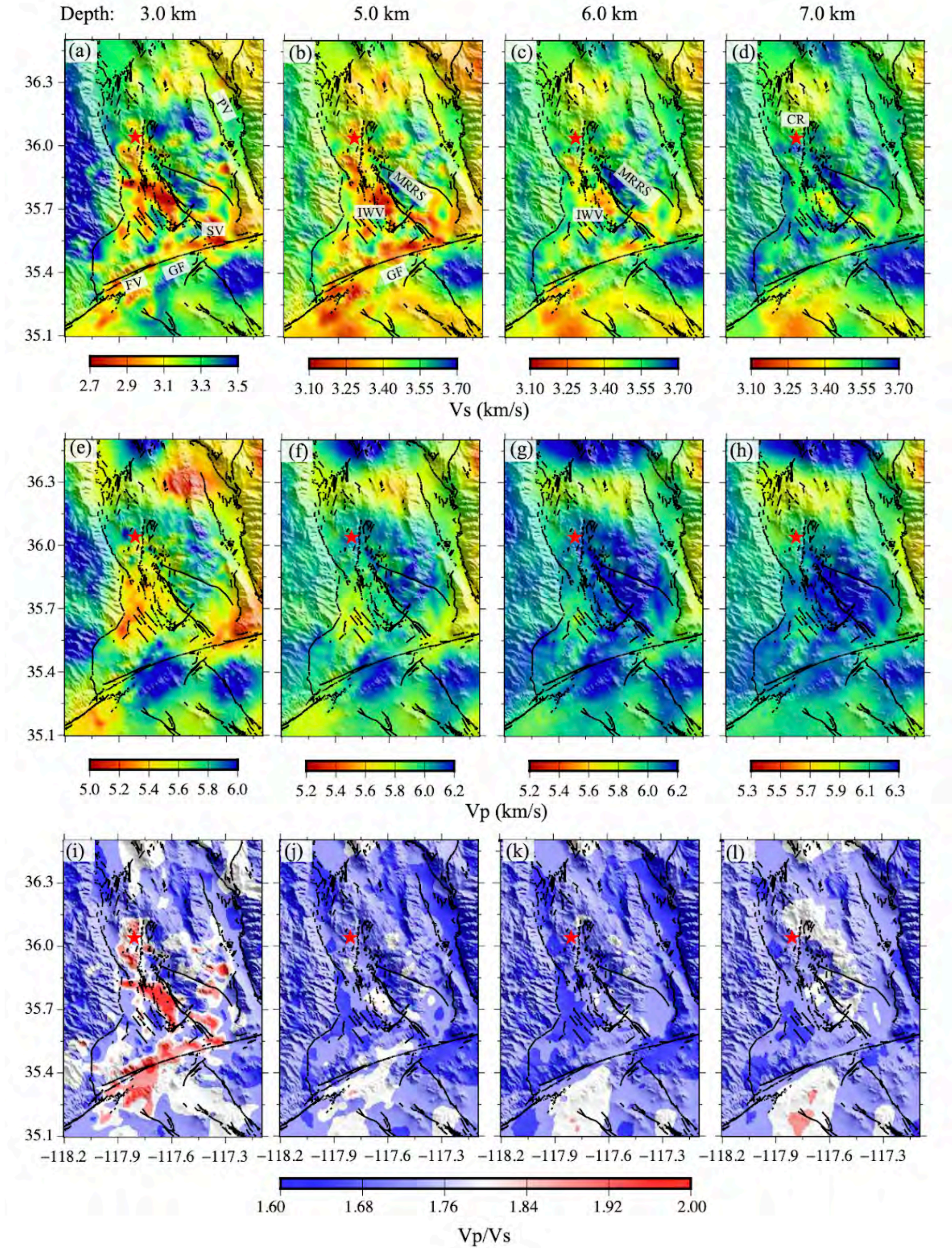

Figure S2: (a)-(l) horizontal cross-sections of Vs, Vp and Vp/Vs at depth of 3 km, 5 km, 6 km and 7 km. Major geological provinces in this region are labeled with abbreviations, including the Indian Wells Valley (IWV), Searles Valley (SV), Fremont Valley (FV), Panamint Valley (PV), Garlock Fault (GF), Main Ruptures of the 2019 Ridgecrest Sequence (MRRS), Mojave Desert (MD) and Coso Range (CR).

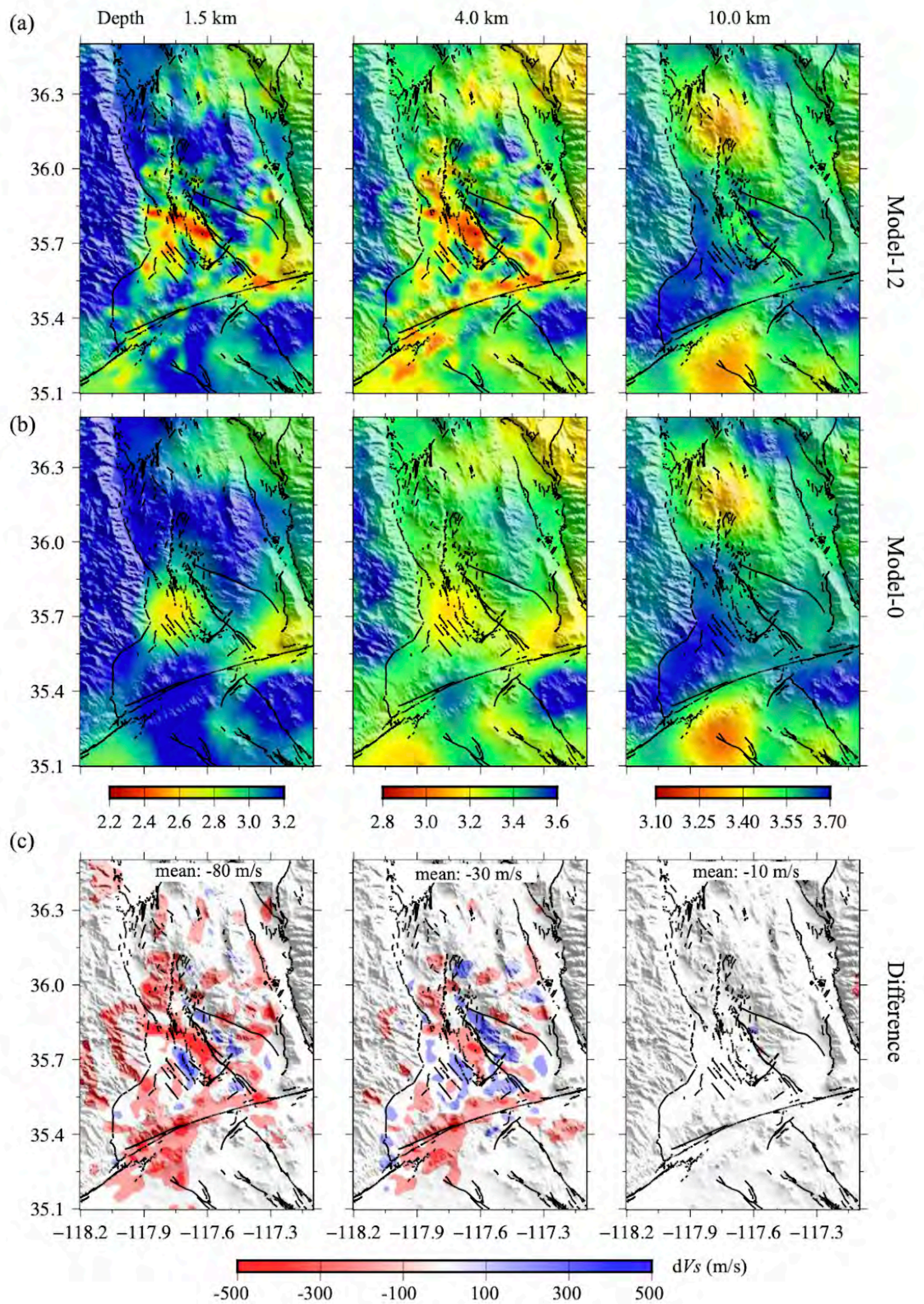

Figure S3: Figures showing Vs differences between the final model-12 and the initial model. Panel (a) shows the Vs at three depths from the Mode-12. Panel (b) shows the Vs at the same depths but from the initial model. Panel (c) Vs discrepancies of two models. The red color means the final model-12 is slower than the initial model. The averaged differences are listed in the upper part of the figures.

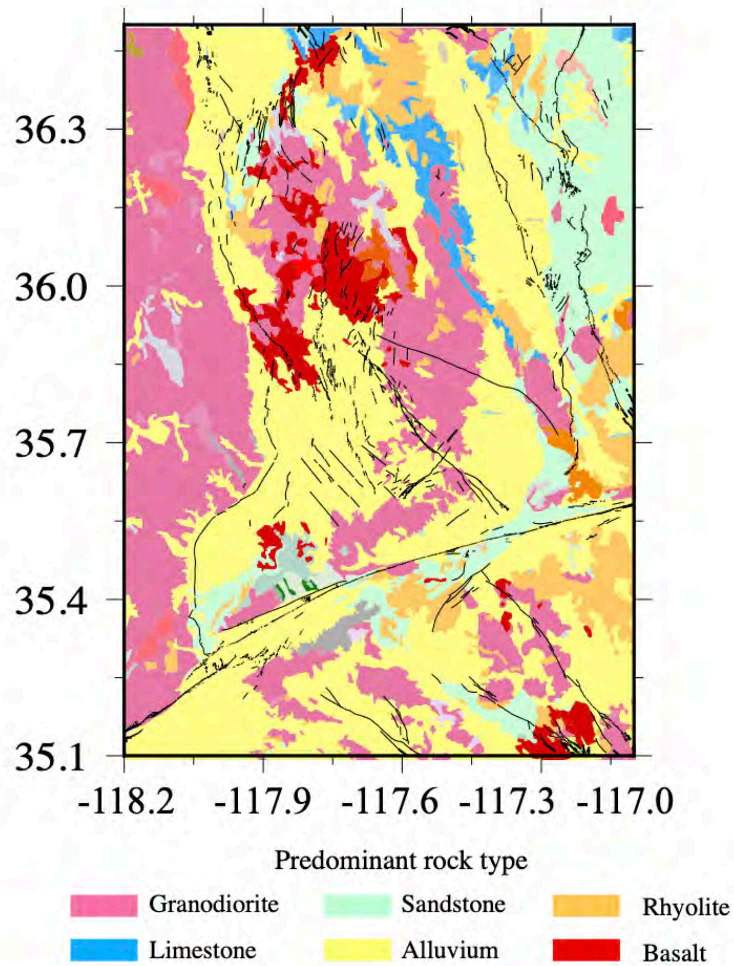

Figure S4: Geological map of surface rock types in the study area.

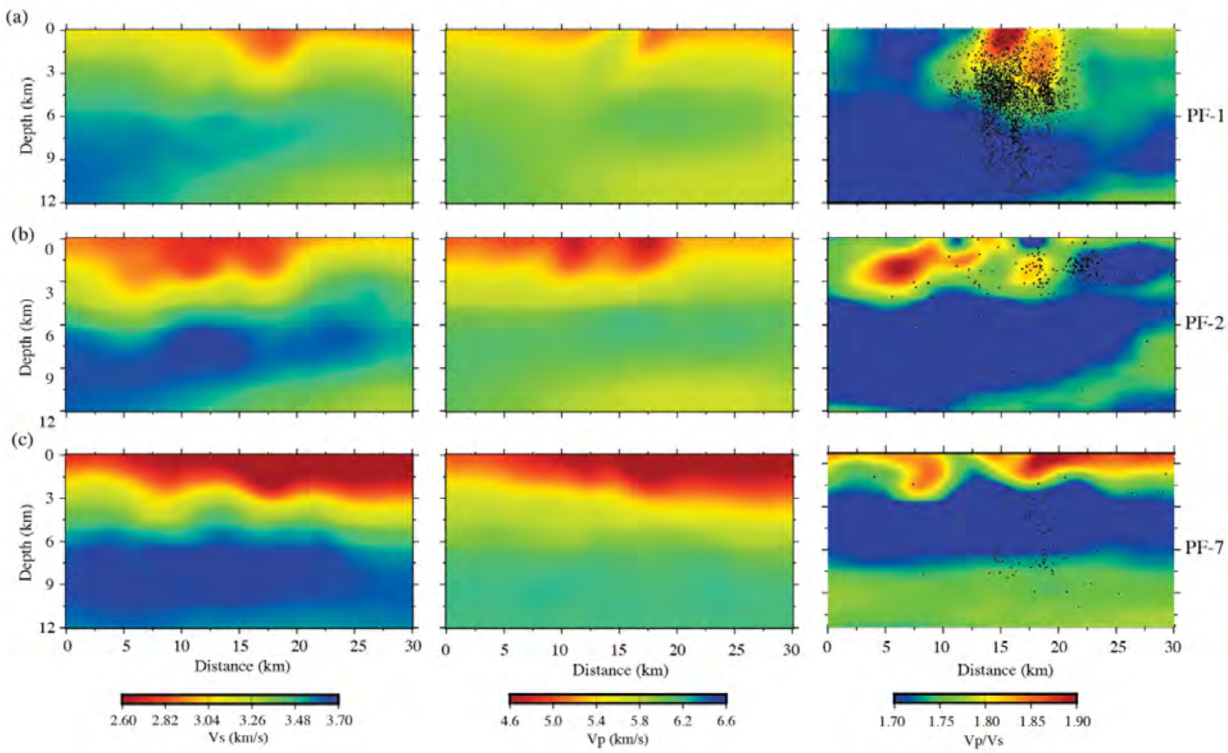

Figure S5: Panels (a) to (c) show four cross-sections of Vs, Vp, and Vp/Vs profiles crossing the main ruptures of the 2019 Ridgecrest Earthquakes. The locations of the four cross-sections are marked in Figure 1b. Events with distances less than 5.0 km from the cross-sections and magnitudes greater than 1.0 are projected onto the Vp/Vs profiles as black dots.

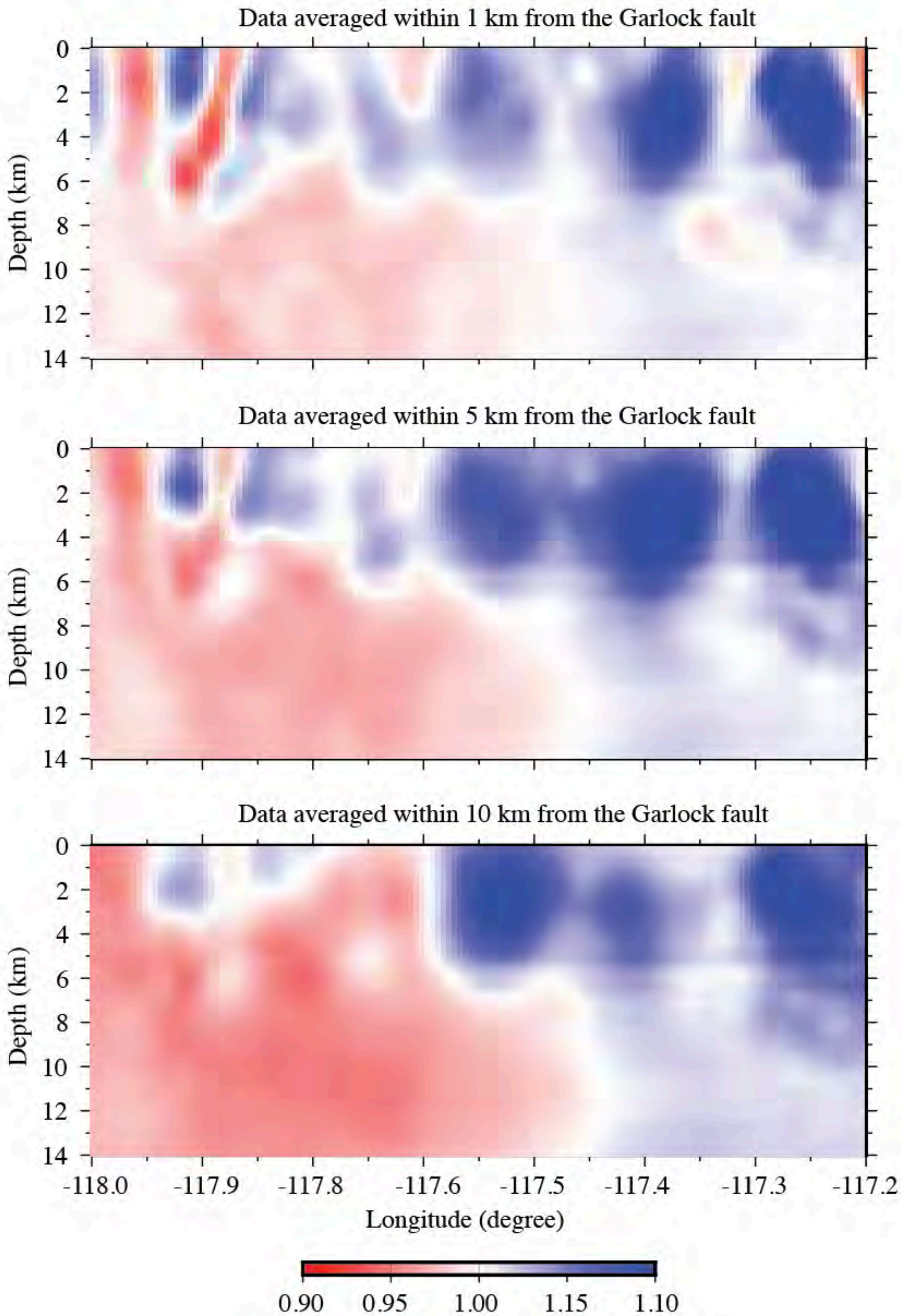

Figure S6: Vs contrast along Garlock Fault calculated from results within 1 km, 5 km and 10 km to the Garlock Fault.